Geochemistry, Geophysics, Geosystems®

AGU ADVANCING EARTH AND SPACE SCIENCES

RESEARCH ARTICLE
10.1029/2023GC011011

Fluid Mixing and Spatial Geochemical Variability in the Lost City Hydrothermal Field Chimneys

Karmina A. Aquino[1,2], Gretchen L. Früh-Green[1], Stefano M. Bernasconi[1], Jörg Rickli[1], Susan Q. Lang[3], and Marvin D. Lilley[4]

[1]Department of Earth Sciences, ETH Zürich, Zürich, Switzerland, [2]Now at Department of Science and Technology, Philippine Nuclear Research Institute, Quezon City, Philippines, [3]Woods Hole Oceanographic Institution, Woods Hole, MA, USA, [4]School of Oceanography, University of Washington, Seattle, WA, USA

Key Points:

- The mineralogy and geochemistry of Lost City chimneys are controlled by the extent of mixing between hydrothermal fluids and seawater
- Brucite and calcite precipitate in vent fluid dominated zones while aragonite forms in the exterior of the structures in seawater-rich zones
- Carbonates precipitate in isotopic disequilibrium and record the O and C stable isotope composition of seawater dissolved inorganic carbon

Supporting Information:

Supporting Information may be found in the online version of this article.

Correspondence to:

K. A. Aquino,
kaaquino@pnri.dost.gov.ph

Citation:

Aquino, K. A., Früh-Green, G. L., Bernasconi, S. M., Rickli, J., Lang, S. Q., & Lilley, M. D. (2024). Fluid mixing and spatial geochemical variability in the Lost City hydrothermal field chimneys. *Geochemistry, Geophysics, Geosystems*, *25*, e2023GC011011. https://doi.org/10.1029/2023GC011011

Received 19 APR 2023
Accepted 18 DEC 2023

Abstract Carbonate-brucite chimneys are a characteristic of low- to moderate-temperature, ultramafic-hosted alkaline hydrothermal systems, such as the Lost City hydrothermal field located on the Atlantis Massif at 30°N near the Mid-Atlantic Ridge. These chimneys form as a result of mixing between warm, serpentinization-derived vent fluids and cold seawater. Previous work has documented the evolution in mineralogy and geochemistry associated with the aging of the chimneys as hydrothermal activity wanes. However, little is known about spatial heterogeneities within and among actively venting chimneys. New mineralogical and geochemical data ($^{87}Sr/^{86}Sr$ and stable C, O, and clumped isotopes) indicate that the brucite and calcite precipitate at elevated temperatures in vent fluid-dominated domains in the interior of chimneys. Exterior zones dominated by seawater are brucite-poor and aragonite is the main carbonate mineral. Carbonates record mostly out of equilibrium oxygen and clumped isotope signatures due to rapid precipitation upon vent fluid-seawater mixing. On the other hand, the carbonates precipitate closer to carbon isotope equilibrium, with dissolved inorganic carbon in seawater as the dominant carbon source and have $\delta^{13}C$ values within the range of marine carbonates. Our data suggest that calcite is a primary mineral in the active hydrothermal chimneys and does not exclusively form as a replacement of aragonite during later alteration with seawater. Elevated formation temperatures and lower $^{87}Sr/^{86}Sr$ relative to aragonite in the same sample suggest that calcite may be the first carbonate mineral to precipitate.

Plain Language Summary At the Lost City hydrothermal field, warm alkaline fluids are discharging out of uplifted mantle rocks. When vent fluids mix with seawater at the seafloor, carbonate and brucite minerals form spectacular towers up to 60 m high. Systems like Lost City are important because the reaction between water and rocks provides carbon and energy sources for microbial life. However, we still do not fully understand what controls the mineralogy and geochemistry of the Lost City hydrothermal chimneys. In this paper, we suggest that the extent of mixing between the hydrothermal fluids and seawater influences the mineralogy and geochemistry of the chimneys. Calcite, which was previously thought to form only during alteration of aragonite by seawater, can also form during seawater-hydrothermal fluid mixing. Both calcite and brucite form in the interior of the chimneys where vent fluid is more dominant. Aragonite, on the other hand, forms in the exterior of the structures from seawater-rich fluids. Lastly, because minerals precipitate rapidly during fluid mixing, the stable isotope geochemistry of the carbonates mostly records the composition and temperature of seawater and not the mixed fluid. Thus, care should be exercised in interpreting mineral geochemical data from similar systems.

1. Introduction

Since the discovery of the Lost City hydrothermal field (LCHF; Kelley et al., 2001), carbonate-brucite deposits associated with low to moderate temperature serpentinite-hosted hydrothermal systems are increasingly being recognized in different tectonic settings and are possibly widespread components of serpentinizing environments on the seafloor. Carbonate-brucite deposits occur at or near slow- and ultraslow-spreading mid-oceanic ridges (Kelley et al., 2001; Lartaud et al., 2011; Lecoeuvre et al., 2020), in subduction forearc regions (Ohara et al., 2012; Okumura et al., 2016), in magma-poor continental margins (Klein et al., 2015; Schwarzenbach, Früh-Green, et al., 2013), and they are also associated with continental ophiolitic settings (Launay & Fontes, 1985; Monnin et al., 2014; Pisapia et al., 2017). High-temperature, black-smoker hydrothermal systems in slow- and ultraslow-spreading environments that are hosted in both mafic and serpentinite basement rocks, such as the Rainbow and

10.1029/2023GC011011

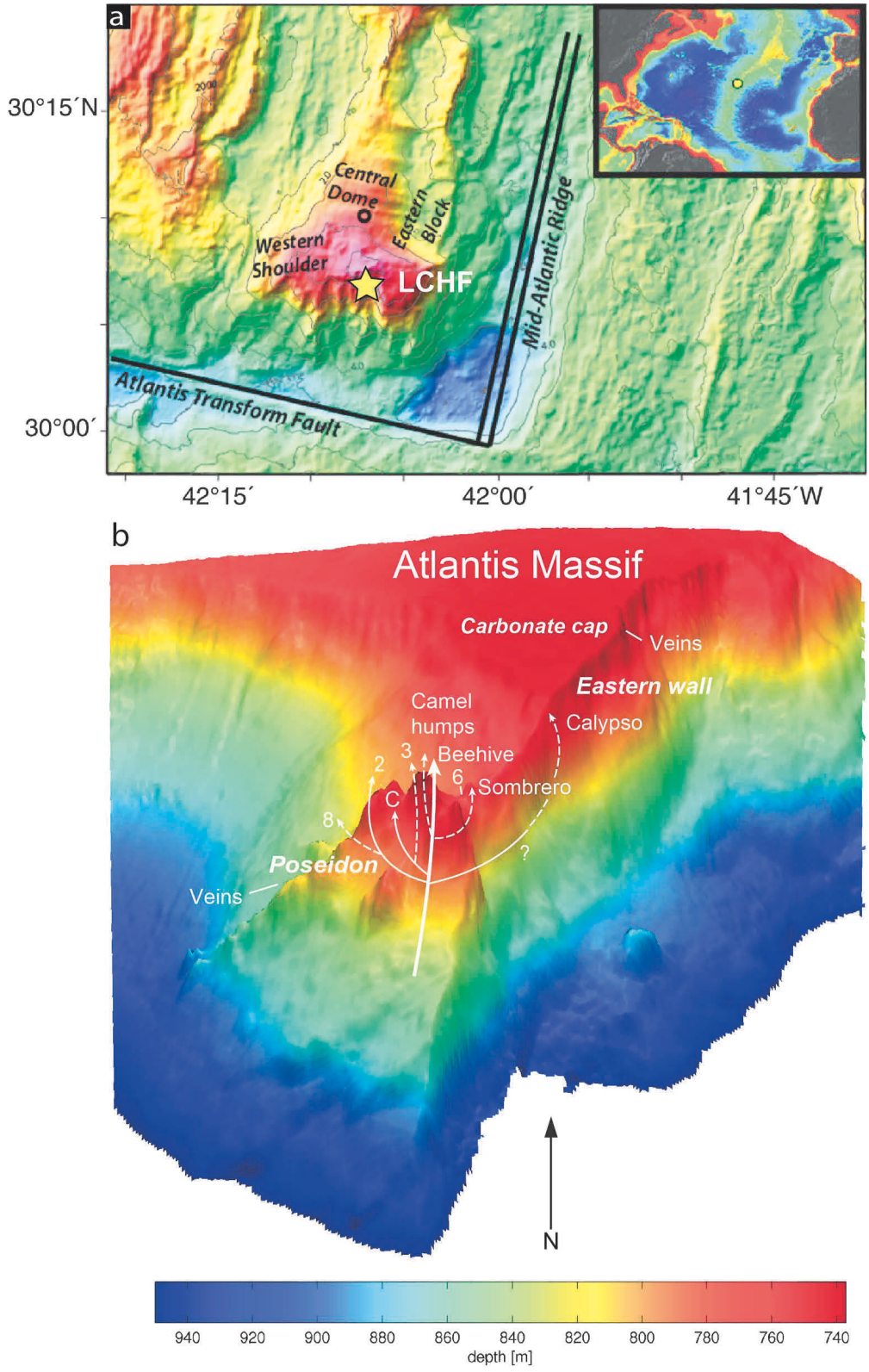

Figure 1.

Logachev hydrothermal fields, are generally characterized by acidic (pH 2–6), metal- and sulfide-rich vent fluids (Charlou et al., 2002; Diehl & Bach, 2020; Douville et al., 2002; Früh-Green et al., 2022; German & Seyfried, 2013; Hannington et al., 2005; Von Damm, 1990). In contrast, fluids derived from Lost City-type systems are relatively cool (~30–120°C), alkaline (pH 9–11), metal- and CO_2-poor, and are rich in dissolved volatiles such as H_2, CH_4, and other short chain hydrocarbons (Cipolli et al., 2004; Eickenbusch et al., 2019; Hannington et al., 2005; Kelley et al., 2005; Lang et al., 2010; Monnin et al., 2014; Proskurowski et al., 2006, 2008; Schwarzenbach, Lang, et al., 2013; Seyfried et al., 2015). Instead of sulfide structures typical of black-smoker systems, delicate carbonate-brucite chimneys form in zones where serpentinization-derived hydrothermal fluids mix with oxygenated, Mg- and CO_2-rich seawater (Früh-Green et al., 2003; Kelley et al., 2001; Ludwig et al., 2006; Okumura et al., 2016; Pisapia et al., 2017):

$$\underset{\text{seawater}}{Mg^{2+}} + \underset{\text{vent fluid}}{2OH^-} \rightarrow \underset{\text{brucite}}{Mg(OH)_2} \quad (1)$$

$$\underset{\text{vent fluid}}{Ca^{2+} + OH^-} + \underset{\text{seawater}}{HCO_3^-} \rightarrow \underset{\text{Ca}-\text{carbonate}}{CaCO_3} + H_2O. \quad (2)$$

Serpentinization occurs when seawater reacts with the mineral olivine to form serpentine (Moody, 1976):

$$\text{olivine} + H_2O \rightarrow \text{serpentine} \pm \text{brucite} \pm \text{magnetite} \pm H_2. \quad (3)$$

The alteration of olivine is associated with the oxidation of Fe^{2+} to Fe^{3+} coupled with the reduction of H_2O to H_2, liberating OH^- ions and producing highly alkaline and reduced fluids that characterize serpentinizing systems such as the LCHF (e.g., Abrajano et al., 1988; Kelley et al., 2001; Lecoeuvre et al., 2020; Neal & Stanger, 1983).

H_2 derived from water-rock reactions during serpentinization may promote the synthesis of some organic molecules from inorganic carbon that may have different sources (Berndt et al., 1996; Lang et al., 2010; McCollom & Seewald, 2007; Proskurowski et al., 2008; Shock & Schulte, 1998; Steele et al., 2022). Abiotic organic compounds including CH_4 may be produced from CO_2 reduction via Fischer-Tropsch-type or Sabatier-type reactions (Charlou et al., 2002; Holm et al., 2015; McCollom & Seewald, 2007; Proskurowski et al., 2008). More recent work emphasizes the formation of CH_4 within olivine-hosted fluid inclusions at depth, which can later be released into the vent fluids during hydrothermal circulation (Grozeva et al., 2020; Kelley & Früh-Green, 1999, 2001; Klein et al., 2019; Labidi et al., 2020; McDermott et al., 2015; Wang et al., 2018). Overall, serpentinization reactions can provide both carbon and energy sources for chemoautotrophy (Amend et al., 2011; Dick & Shock, 2021; Früh-Green et al., 2004; Lang & Brazelton, 2020; McCollom, 2007; McCollom & Seewald, 2007), are likely to have been widespread in the early Earth (Sleep, 2010), and could potentially be occurring in other planetary bodies such as Enceladus and Europa (Glein et al., 2015; McKay et al., 2008; Waite et al., 2017). Therefore, systems like the LCHF can improve our understanding of the geochemical evolution of life on Earth and elsewhere.

The LCHF is the first documented and remains the best studied example of such low temperature marine hydrothermal systems to date. It is located approximately 15 km west of the Mid-Atlantic Ridge (MAR) at 30°N at the inside corner of the intersection with the Atlantis Transform Fault (Figure 1). The field is at the top of a terrace on the southern wall of the Atlantis Massif at about 700–800 m below sea level. At least 30 carbonate-brucite structures (Figure 2), up to 60 m high, span across the approximately 500 m^2 vent field and include actively venting and inactive spires, pinnacles, parasitic flanges, and veins (Kelley et al., 2001). Ludwig et al. (2006, 2011)

Figure 1. Location of the Lost City hydrothermal field (LCHF) and the vent sites investigated in this study. (a) Overview of the LCHF situated on the southern wall of the Atlantis Massif at 30°N west of the Mid-Atlantic Ridge (Blackmann et al., 2002). (b) 3-Dimensional map of the LCHF (after Kelley et al. (2005)) including the vents studied here. The massive 60-m structure Poseidon is a composite of multiple active vents in the center of the field. Active vents are also found along the northeast trending escarpment called the eastern wall. Carbonate veins were collected close to the eastern wall and west of Marker 8. Also shown are inferred vent fluid flow paths showing the relationship between vent sites after Aquino et al. (2022): thick solid line, first order vent—Beehive; thin solid line, second order vents—Marker C and Marker 2; thin dashed lines, third order vents.

10.1029/2023GC011011

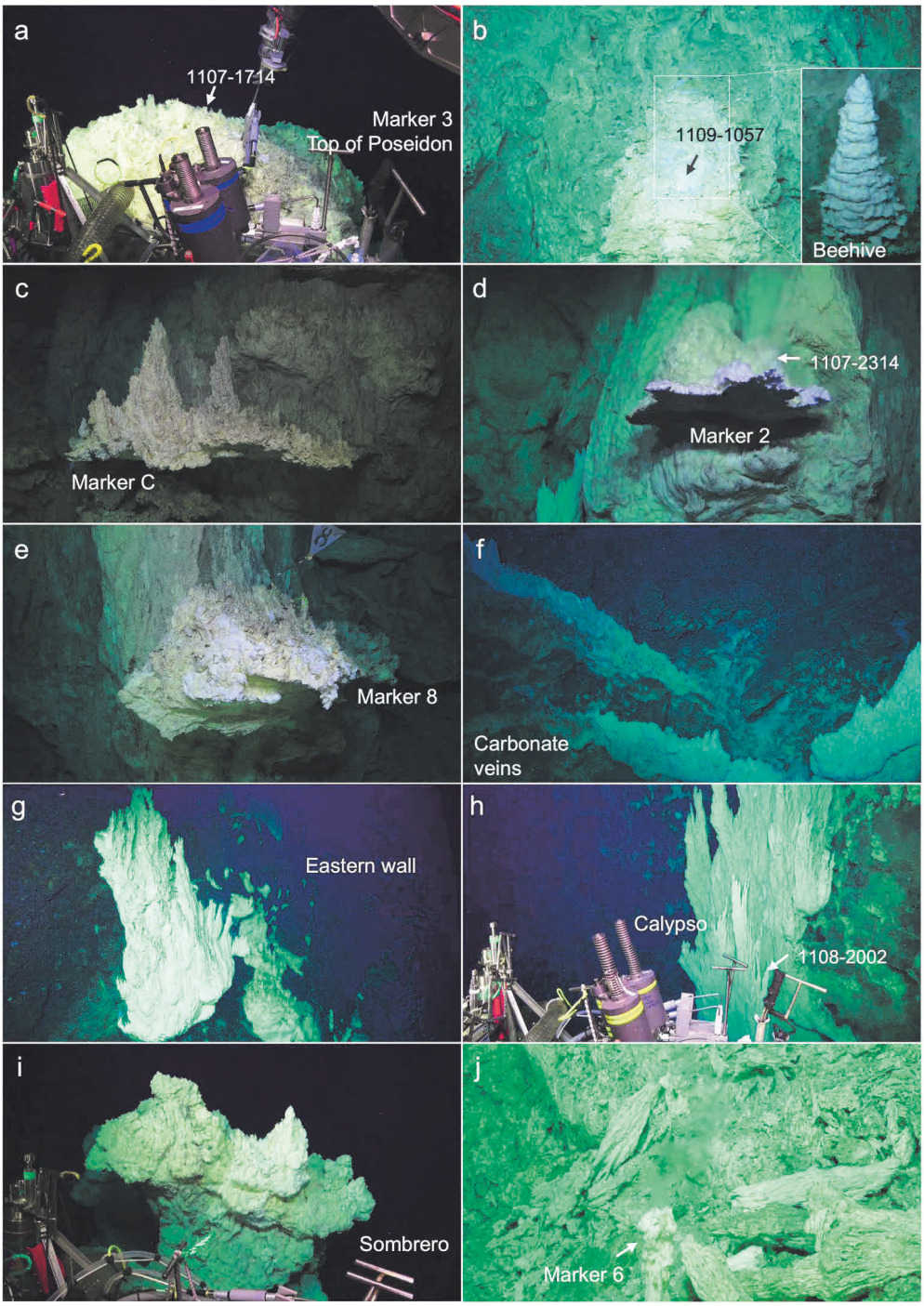

Figure 2. Dive images of vent sites investigated. (a) Marker 3 located at the top of the Poseidon structure. (b) Location of active venting at what used to be the Beehive structure. White box indicates the general location of the Beehive structure and inset shows the structure in 2005 (Kelley et al., 2005). (c) Marker C flange. (d) Marker 2 or IMAX flange. (e) Marker 8 flange. (f) Carbonate veins or fissure-filling deposits located west of Marker 8. (g) Carbonate spires along the eastern wall. (h) Calypso spire, located along the eastern wall. White arrow points to the spire collected as sample 1108–2002. (i) Top of the Sombrero structure. (j) Marker 6 spire. Images courtesy of S. Lang, UofSC/NSF/remotely operated vehicle Jason/2018 © WHOI.

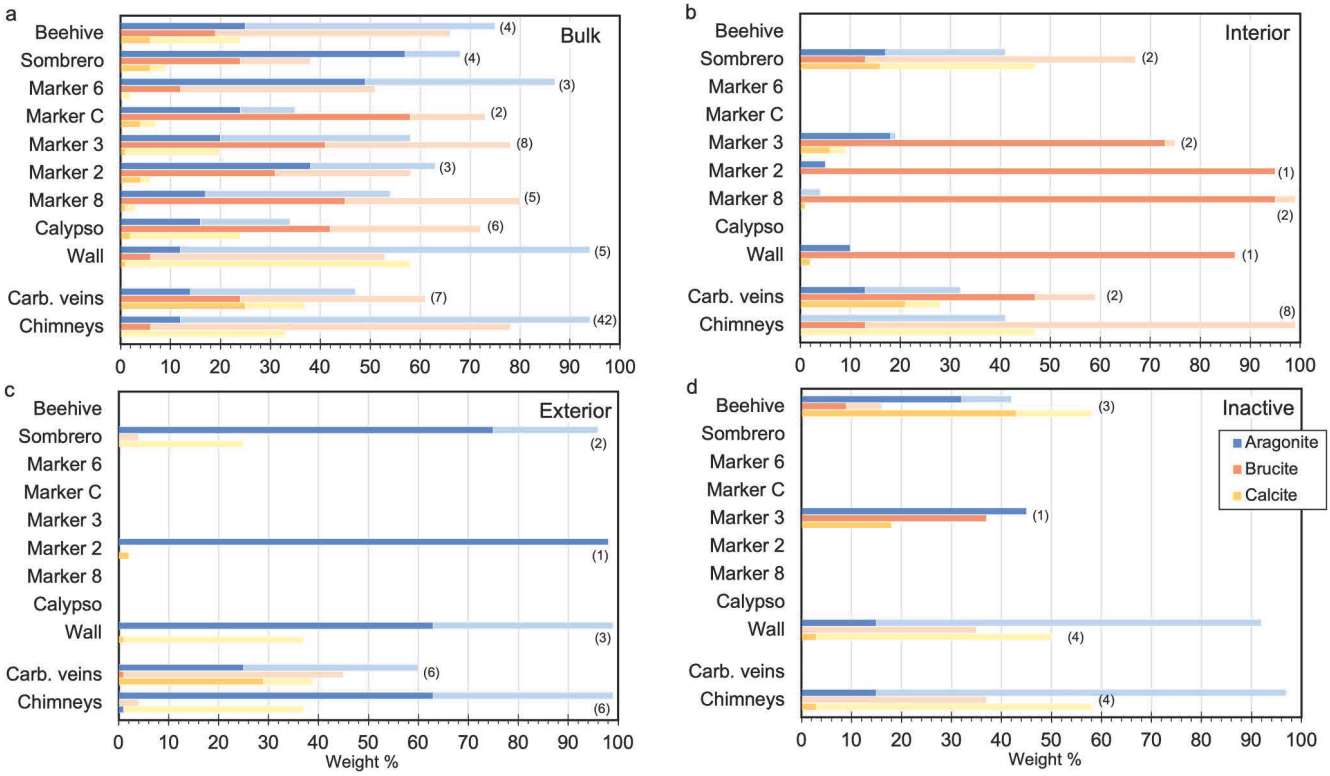

Figure 3. Mineral abundances of samples collected at each site. (a) Subsamples representative of the bulk sample. (b) Chimney interior. (c) Chimney exterior. (d) Inactive chimneys. Notes: Number of samples analyzed for each site is shown in parentheses. Blue = aragonite; orange = brucite; yellow = calcite. Dark and light shades represent minimum and maximum mineral abundances, respectively. Data from Aquino et al. (2024). Samples classified as "inactive" from the active structures Beehive and Marker 3 are older parts of the chimney that are yellowish and show a higher degree of induration and form the substrate for new bright white chimney growth.

extensively studied the mineralogical, geochemical, and textural transformation during aging of the chimneys from nascent to inactive and extinct structures. They documented that young, active chimneys precipitate predominantly as aragonite and brucite, characterized by low $^{87}Sr/^{86}Sr$ and low trace element contents. Progressive reaction with seawater results in the conversion of aragonite to calcite and dissolution of brucite, as well as increases in $^{87}Sr/^{86}Sr$ and trace element concentrations (Ludwig et al., 2006). In addition to heterogeneities attributed to aging of the chimneys, spatial variabilities in temperature, chemistry, and microbial activity across the field as well as within a single structure were documented at the LCHF (Brazelton et al., 2006; Schrenk et al., 2004). Active vents in the central part of the field have higher temperature, higher H_2 and SO_4^{2-} concentrations, and lower H_2S and lower amount of biomass than those found at the periphery (Lang et al., 2012; Proskurowski et al., 2006). Previous studies have reported systematic differences in terms of mineralogy and geochemistry between the interior and rim of a single chimney (Ludwig et al., 2006, 2011; Vogel, 2016). In our companion paper (Aquino et al., 2024), we show that calcite is associated with brucite and occurs in the interior of actively venting spires as well as the downward-facing side of flanges. In contrast, aragonite generally comprises the exterior of the chimneys (Figure 3). The mechanism behind these observed spatial heterogeneities in the mineralogy remains uncertain.

The objective of this study is to understand the controls on the spatial variations observed in the mineralogy of the active chimneys. Our geochemical data show that heterogenous precipitation conditions (e.g., pH, temperature, Mg/Ca ratios) at Lost City are largely controlled by the variability in mixing proportions of vent fluid and seawater, which affects the mineralogy and geochemistry of the resulting hydrothermal chimneys. Stable carbon and oxygen isotope data suggest that during the very rapid precipitation of carbonate upon fluid mixing, the dissolved inorganic carbon (DIC) behaves as a closed system preventing equilibration between DIC, which is mostly sourced from seawater, and H_2O or OH^-. As a result, the carbonates record oxygen and clumped isotope compositions that do not reflect the temperature of the formation fluid.

2. Sampling Sites

The locations of the sampled vent structures are shown in Figure 1 and listed in Table S1 of Supporting Information S1. Here we briefly summarize the morphology of the structures which has been discussed in previous studies (Früh-Green et al., 2003; Kelley et al., 2001, 2005; Ludwig et al., 2006). We use location names described in earlier studies and names of field markers deployed during previous sampling campaigns (e.g., Kelley et al., 2005, Figure S1 in Supporting Information S1; Lang et al., 2010; Ludwig et al., 2006; Proskurowski et al., 2006). Carbonate-brucite chimneys occur in a wide variety of morphologies. The central and most prominent part of the field is the 60-m high Poseidon structure, which is a composite of actively venting towers and spires including Marker 3 and Camel humps, and parasitic vent structures forming cone- and flange-like morphologies (Figures 1 and 2). The Beehive vent is a ∼1-m high, cone-like parasitic structure that vents the hottest fluid (up to 96–116°C; Table S1 in Supporting Information S1), which can be considered the primary, unaltered endmember fluid at LCHF (Aquino et al., 2022; Kelley et al., 2005; Ludwig et al., 2006; Seyfried et al., 2015). The structure itself was no longer present during our sampling in 2018, but we were able to collect chimney samples from a venting orifice, presumably representing the interior of the former structure (Table S2 in Supporting Information S1, Figure 2b). Marker C and Marker 2 (also called IMAX flange), are parasitic flanges on the Poseidon structure, which include horizontally growing structures that trap warm vent fluids (Figures 2c and 2d). In some cases, chimney spires grow on the top of these flanges. We also sampled Marker 8 (Figure 2e), another parasitic flange west of Poseidon, as well as several veins or fissure filling carbonate-brucite deposits located west of Marker 8 (Figure 2f).

The eastern wall is a steep escarpment where carbonate veins and morphologically diverse chimney structures (Figure 2g) grow directly along faults or subhorizontal foliations in the serpentinites (Kelley et al., 2005). It is located along a ridge extending toward the northeast from the main vent field (Figure 1). We sampled several structures, including actively venting spires such as Calypso (Figure 2h), and others that showed no evidence of venting at the time of sampling. Veins that crosscut the relatively flat-lying carbonate-cap sedimentary sequences at the top of the southern Atlantis Massif (Kelley et al., 2005) were also sampled. Marker 6 and Sombrero are two sites located east of Poseidon and close to the eastern wall. Sombrero is an actively venting spire with fresh growth at the top of the structure (Figure 2i). The structure on Marker 6 on the other hand is a small, delicate, actively venting spire that grew atop the rubble of inactive chimneys (Figure 2j). Despite their location away from Poseidon at the center of the field, these vents are thought to share a common flow path with Beehive (Figure 1b; Aquino et al., 2022; Seyfried et al., 2015).

3. Materials and Methods

3.1. Samples

Grab and suction (slurp) samples of hydrothermal chimneys and fissure-filling veins were collected with the remotely operated vehicle (ROV) *Jason* during the Lost City 2018 Return expedition (*R/V Atlantis* cruise AT42-01). Chimney samples were mostly obtained in sites where active venting, recognized primarily by shimmering water and increased water temperatures, was observed. During six dives (Dives 1107 to 1112), we sampled sites that had been previously investigated (Figure 1), such as Beehive and sites named after field markers laid out in 2003 (e.g., Marker 2, Marker C; Kelley et al., 2005). Most of these vents are associated with the massive Poseidon structure at the center of the field (Figure 1). Other active vents along the eastern wall were sampled for the first time in 2018. A total of 31 chimneys and 6 vein samples were collected and described macroscopically. These samples were assigned a unique ID including the *Jason* dive number, the date and time of collection, and the sample type (e.g., J.1109.19Sep.0756 CHIM for a chimney sample collected on 19 September 2018, 07:56 GMT during *Jason* Dive 1109). In this paper, we use a shortened version of the sample ID, which includes the dive number and time of collection (e.g., 1109-0756). Each sample was subdivided onboard into aliquots and distributed among the science party members. Each of these samples was assigned a unique cruise ID (e.g., sample 1109-0756 is further subdivided into samples with cruise ID LC01349, LC01353, etc.). Specimens that exhibited heterogeneities such as distinct colors, textures, or layers were subsampled to analyze their mineralogy and geochemistry (e.g., LC01349a, LC01349b). Samples representing a general average or bulk composition of a chimney or vein were also analyzed separately. Mineral separation via hand picking was carried out on selected samples to determine texture- and/or mineralogy-specific isotopic compositions.

3.2. Analytical Methods

A total of 76 samples from 31 chimneys and 6 carbonate veins were analyzed for mineralogy, chemistry, and stable C and O isotope compositions, 33 for $^{87}Sr/^{86}Sr$ ratios, and 24 for carbonate clumped isotopes (Δ_{47}). 14 and 12 mineral separates were also measured for their $^{87}Sr/^{86}Sr$ and Δ_{47} values, respectively. For major and trace element analyses, powdered samples were washed with distilled water and centrifuged several times to remove salt and dirt, and subsequently freeze dried. 300 µg of sample material were then dissolved in 300 µl of 2% HNO_3 and measured on an Agilent 8800 Triple Quadrupole inductively coupled plasma mass spectrometer (ICP-MS) at the Geological Institute, ETH Zürich.The precision of the analyses is better than ∼5% (RSD) based on repeated analyses of standards.

Carbon and oxygen isotope analyses were conducted on 90–140 µg of carbonates (powdered and washed) using a GasBench II system coupled with a Delta V isotope ratio mass spectrometer (IRMS, Thermo Fischer Scientific, Bremen, Germany) at the Geological Institute, ETH Zürich following the methodology of Breitenbach and Bernasconi (2011). Results are reported in the conventional delta notation relative to the Vienna Pee-Dee Belemnite (VPDB). The average standard deviation of repeated measurements of standards during different sessions is less than 0.1‰ for both $\delta^{18}O$ and $\delta^{13}C$. Carbonate oxygen isotope thermometry is a widely used technique to determine the temperature at which carbonate minerals precipitate based on the temperature-dependent fractionation between carbonate and water. Given the $\delta^{18}O$ of the formation water and the measured $\delta^{18}O$ of the carbonate, the temperature of precipitation may be estimated (Urey et al., 1951). Here, the $\delta^{18}O$-based precipitation temperatures were calculated using the calibration of O'Neil et al. (1969) as recalculated by Friedman and O'Neil (1977).

Carbonate clumped isotope thermometry is a powerful geochemical method to estimate the temperature of formation of carbonate minerals. This technique is based on the temperature-dependent abundance of ^{13}C-^{18}O bond within the carbonate lattice and is thus independent of the isotopic composition of the formation water, unlike the oxygen isotope thermometer (Ghosh et al., 2006; Schauble et al., 2006). Carbonate clumped isotope analyses were performed using a Kiel IV carbonate device coupled to a 253Plus IRMS (both Thermo Fisher Scientific) at the Geological Institute, ETH Zürich as described by Meckler et al. (2014) and Müller et al. (2017). The carbonate samples reacted with three drops of 104% H_3PO_4 at 70°C via the Kiel IV device. The CO_2 gas released from this reaction was then purified in a custom-built Porapak Q resin held at −40°C to remove potential isobaric contaminations. Samples were measured with a maximum of three replicate measurements per sample and session, which generally consists of 24 measurements of 100–120 µg sample carbonate interspersed with 5 replicates each of the carbonate standards ETH-1, ETH-2 and 10 replicates of ETH-3 (Bernasconi et al., 2018, 2021). The samples were analyzed in LIDI mode with 400 s of integration of sample and reference gas. Raw data processing and background corrections were performed using the Easotope software (John & Bowen, 2016). Sample compositions are reported as the excess abundance of the CO_2 isotopologue with mass 47 relative to the abundance expected from a random distribution of isotopes:

$$\Delta_{47} = \frac{R^{47}}{R^{47*} - 1}, \tag{4}$$

where R^{47} is the ratio of the abundance of the CO_2 isotopologue with mass 47 relative to the abundance of the most common CO_2 isotopologue with mass 44 and R^{47*} is the ratio expected from a random distribution calculated from the measured $\delta^{13}C$ and $\delta^{18}O$ values. Sample Δ_{47} measurements were converted to the Δ_{47} Intercarb-Carbon Dioxide Equilibrium Scale (Bernasconi et al., 2021) using the ETH-1, ETH-2 and ETH-3 carbonate standards described previously (Bernasconi et al., 2018; Meckler et al., 2014; Müller et al., 2017) with the community-derived Δ_{47} values reported by Bernasconi et al. (2021). Δ_{47}-based temperatures were calculated using the calibration of Anderson et al. (2021).

Radiogenic Sr isotope and Sr concentration analysis were performed at the Institute of Geochemistry and Petrology, ETH Zürich. Twenty to thirty mg of powdered carbonate (bulk samples, separated aragonite or calcite) was first reacted in 5 ml of ammonium acetate buffered to pH 5 to leach the carbonate fraction. Leached sample fractions were subsequently dried down and measured dilute for Sr concentrations by ICP-MS (Element XR, Thermo Fisher Scientific). 200–500 ng of Sr was separated from the carbonate matrix using Sr spec resin

following the methods of de Souza et al. (2010) and Deniel and Pin (2001). Strontium isotope ratios ($^{87}Sr/^{86}Sr$) were measured at Sr concentrations of ∼100 ppb on a multicollector ICP-MS (Neptune Plus, Thermo Fischer Scientific). Instrumental mass fractionation was corrected using the exponential law and $^{86}Sr/^{88}Sr$ of 0.11940 (Nier, 1938). The uncertainty of the measurements estimated from repeated measurements of NIST SRM 987 is <24 ppm (2 SD, $n = 15$ per session). Sample $^{87}Sr/^{86}Sr$ values were renormalized to the accepted value of NIST SRM 987 ($^{87}Sr/^{86}Sr = 0.710248$, Thirlwall, 1991).

3.3. Geochemical Calculations

Calculations were performed to simulate the effect of mixing of endmember hydrothermal vent fluids and seawater using the Geochemist's Workbench React Program (Bethke et al., 2020). We used the default thermodynamic database (thermo.tdat), which is based on the LLNL thermochemical database developed at the Lawrence Livermore National Laboratory (Delany & Lundeen, 1990). In the model, the precipitation of calcium carbonate and brucite was simulated as seawater was gradually mixed with 1 kg of hydrothermal fluid. The compositions of the vent fluid and seawater used in the calculations are listed in Table S5 of Supporting Information S1. The calculations done here do not account for the kinetic inhibitions to calcite precipitation by Mg ions (Bischoff, 1968) and thus cannot be used to determine which carbonate polymorph precipitates; both calcite and aragonite precipitate when the formation of the other mineral is suppressed in the calculations. We used the calculated fluid Mg/Ca ratio to qualitatively infer the carbonate mineralogy (see Section 5.2 for more details).

4. Results

The mineralogy of the samples, summarized in Figure 3, is discussed in detail in the companion paper (Aquino et al., 2024). The Lost City chimneys are composed of variable mixtures of aragonite, brucite, and calcite (Figure 3a). In general, the interior of these chimneys is composed mostly of brucite and minor calcite/aragonite (Figure 3b), while the exterior is dominated by aragonite (Figure 3c). Scanning electron microscopy of samples from the interior of the chimneys highlighted the spatial association between brucite and calcite (Aquino et al., 2024). Several samples from relatively high temperature vents (e.g., Beehive and Sombrero) as well as from eastern wall sites (Calypso and carbonate veins) contain significant amounts of calcite (>20%). Many samples exhibit flow textures preserved as brucite mineral membranes upon which aragonite or calcite may precipitate on. In the following section, we compare the results of our geochemical analyses (Tables S2 and S3 in Supporting Information S1) with the mineralogical study presented in Aquino et al. (2024).

4.1. Major and Trace Elements

The major and trace element compositions of the samples are shown in Figure 4. In general, variations in Ca, Mg, and Sr concentrations (Figures 4a and 4b) roughly reflect the relative proportion of carbonate and brucite in the chimneys, consistent with previous studies (Ludwig et al., 2006; Vogel, 2016). The brucite-rich chimney interiors contain up to 40 wt% Mg, whereas the carbonate-rich exteriors and inactive chimneys contain up to 45 wt% Ca (Figure 4a). Brucite does not appear to incorporate significant Sr because the Sr contents of the brucite-rich (>95 wt% brucite, >30 wt% Mg) samples are low (70–237 ppm). In comparison, the chimney exteriors have more than 4,000 ppm Sr, reflecting a higher proportion of aragonite (Figure 4b). Inactive structures contain even more elevated amounts of Sr (up to about 19,000 ppm). Interestingly, most carbonate veins and samples from the eastern wall and Beehive show elevated Si and Al contents (>6,000 ppm and 1,000 ppm, respectively) relative to samples from other sites (<5,000 ppm Si, <1,000 ppm Al). These values are similar to the average marine carbonate sedimentary rock and lower than those of the average marine unlithified carbonate sediments (Figures 4c and 4d). Most trace element (Cr, Mn, Ni, Fe, Zn, Pb) concentrations are significantly lower than those of the average marine carbonate rock and sediments (Figure S1 in Supporting Information S1). On the other hand, Sr, Cd, U, P, and Si have similar or slightly higher concentrations relative to the average marine carbonate rock and carbonate sediments (Figure S1 in Supporting Information S1). Ba, U, P, and S show a generally increasing trend with decreasing Mg, while Zn roughly increases with Mg (Figure S1 in Supporting Information S1).

4.2. Oxygen Isotopes

The Lost City chimney carbonates are isotopically variable and show within-sample heterogeneity at the 100 μg sample size used for the measurements (Figure 5). The $\delta^{18}O$ of mixed calcite and aragonite bulk

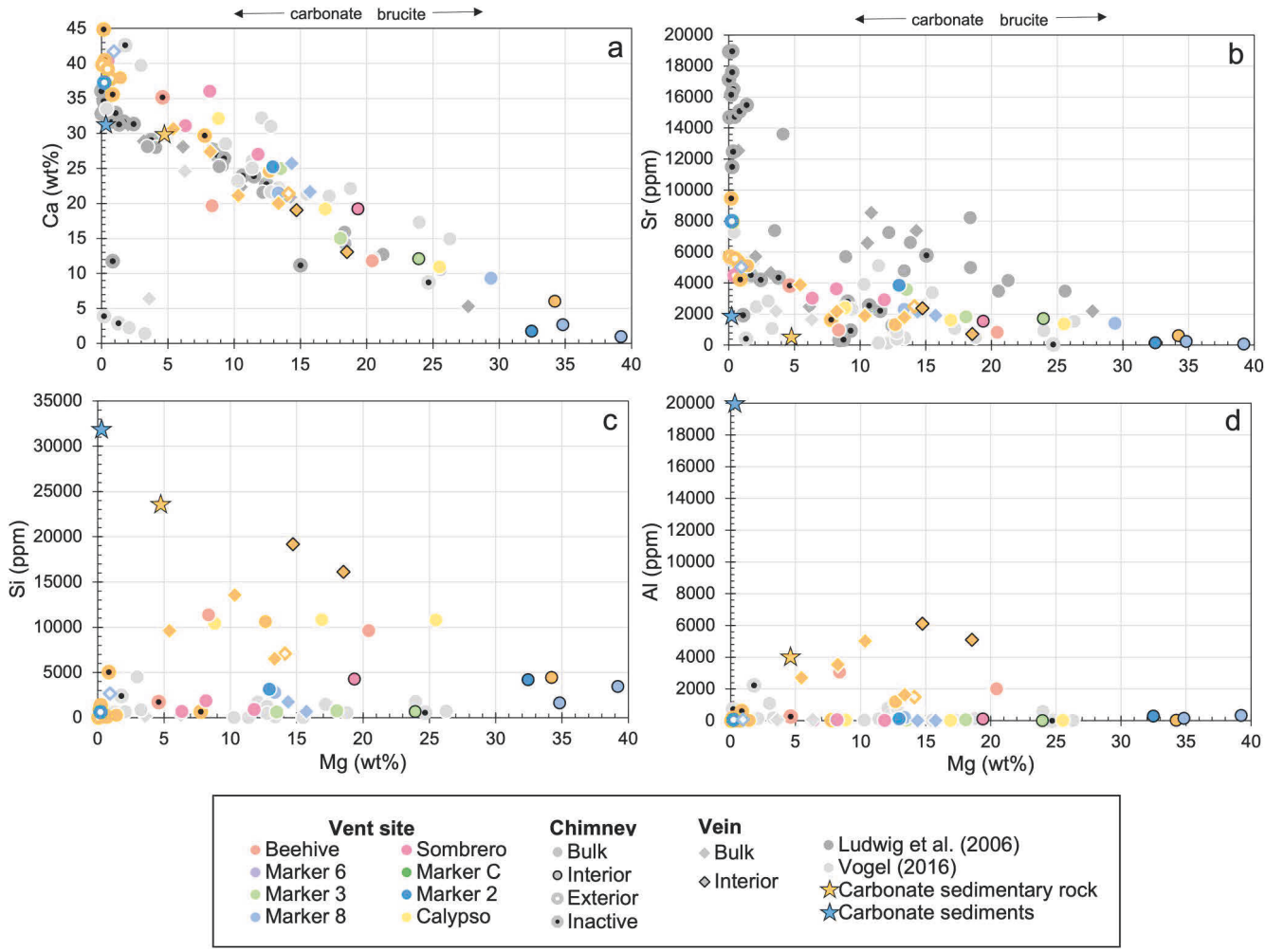

Figure 4. Major element concentrations versus Mg of active carbonate chimneys and fissure filling veins, including data from Ludwig et al. (2006) and Vogel (2016). (a) Variation in Ca and Mg generally reflects the relative proportions of carbonate and brucite in the samples. Note that the interior of the chimneys are generally Mg-rich relative to the exterior. (b) Sr contents increase with increasing Ca and decreasing Mg concentrations. Active structures have significantly lower Sr contents than the inactive chimneys. (c and d) Most samples have minor amounts of Si and Al except for a few samples from the eastern wall and Beehive. Data for marine carbonate sedimentary rock and unlithified marine carbonate sediments are from Turekian and Wedepohl (1961).

samples of active chimneys span a wide isotopic range from −12.45 to 4.67 ‰ (111 analyses of 35 samples) whereas the veins have a narrower range from 1.99 to 5.29 ‰ (116 analyses of 10 samples) (Figure 5a; Table S2 in Supporting Information S1). Beehive, Sombrero, and Marker 6, which belong to the vent group with the lowest dissolved sulfide concentrations of 0.3–0.4 mmol/kg (Aquino et al., 2022), have the lowest and most variable bulk $\delta^{18}O$ values (−12.45 to +3.49‰; 62 analyses of 10 samples). The interior of the chimneys and veins from the same site have similar or lower $\delta^{18}O$ than the bulk, whereas samples from the exterior have similar or higher $\delta^{18}O$ than the bulk (e.g., Figure 5; Figures S2b, S2e, and S2f in Supporting Information S1). The $\delta^{18}O$ of inactive structures are generally similar to those of the active ones (Figures S2a, S2e, and S2i in Supporting Information S1). The $\delta^{18}O$ of calcite crystals and aggregates separated by hand picking ranges between −12.0 and +2.5‰ (n = 54) whereas aragonite $\delta^{18}O$ values are −3.8 to +4.0‰ (n = 85) (Tables S3 and S4 in Supporting Information S1; Figures 5b and 5c). Within each site, calcite $\delta^{18}O$ values are generally lower than or similar to the values of the mixed samples (Figures S2a, S2b, S2d, and S2e in Supporting Information S1). $\delta^{18}O$ values of separated aragonites are mostly similar to or slightly higher than the bulk compositions (Figures S2a–S2g in Supporting Information S1). Except for a few fissure-filling deposits, the oxygen isotope composition of samples collected in 2018 is similar to those reported previously (Figure 5c) (Früh-Green et al., 2003; Vogel, 2016).

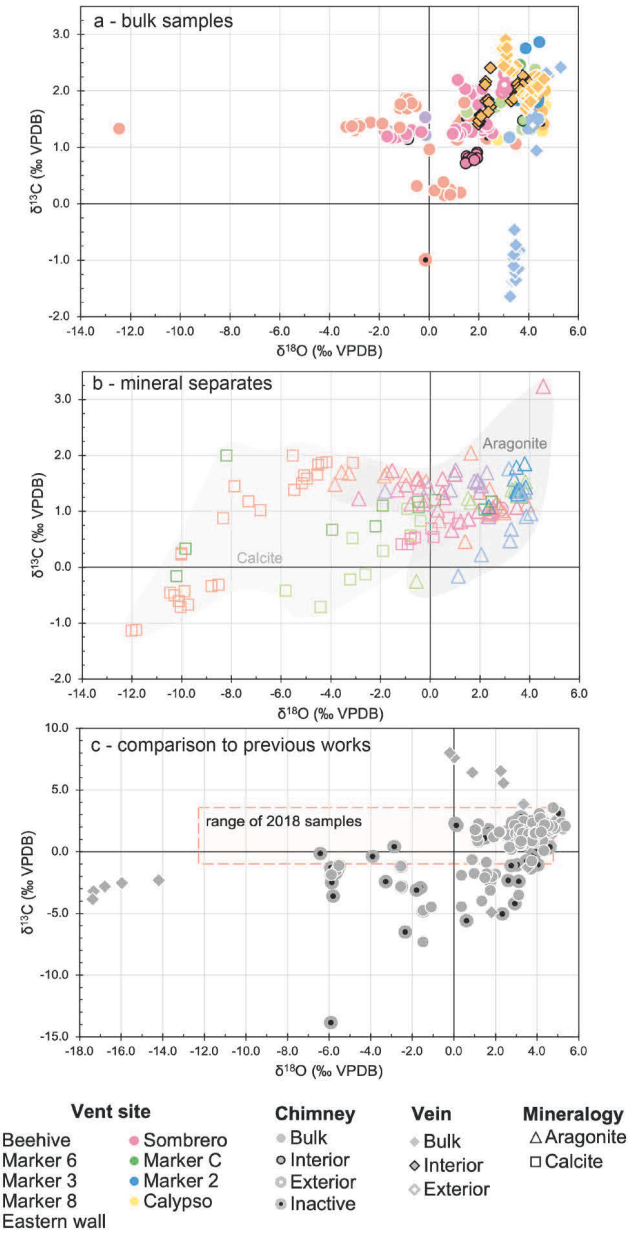

Figure 5. Carbon and oxygen isotope compositions of the Lost City hydrothermal chimneys and veins: (a) bulk samples and (b) mineral separates. Gray fields indicate the range of compositions of calcite and aragonite crystals. (c) Comparison of samples collected in 2018 (mostly active samples) and previous work (active, inactive, fissure filling) (Früh-Green et al., 2003; Vogel, 2016).

4.3. Carbon Isotopes

The bulk $\delta^{13}C$ of the active chimneys (0.15–2.46‰; $n = 101$, Figure 5, Table S2 in Supporting Information S1) lie within a narrower range than the $\delta^{18}O$. Although the inactive chimneys generally have slightly higher bulk $\delta^{13}C$ values (1.52–2.26‰; $n = 25$), these isotope compositions still lie within the range of active chimneys (Figures S2a, S2e, and S2i in Supporting Information S1). Most of the veins (0.94–2.91‰; $n = 102$) have $\delta^{13}C$ values very similar to the chimneys except for one vein west of Marker 8 (average $\delta^{13}C = -1.06$‰; Table S2 in Supporting Information S1, Figure 5a, and Figure S2j in Supporting Information S1). As with $\delta^{18}O$, for samples from the same site, subsamples from the interior of the chimneys have similar or slightly lower $\delta^{13}C$ than the bulk, while subsamples from the exterior of the chimneys have similar or slightly higher $\delta^{13}C$ values than the bulk (Figures S2b, S2e, and S2j in Supporting Information S1). Both pure calcite and aragonite have $\delta^{13}C$ values that lie in a relatively wide range between −1.1 and +2.0‰ ($n = 54$) and between −0.3 and +2.0‰ ($n = 85$), respectively. The average $\delta^{13}C$ for calcite is lower than for aragonite (Tables S3 and S4 in Supporting Information S1). The carbon isotope composition of LCHF samples reported in earlier studies spans a wider range than those of samples collected in 2018 (Figure 5c) (Früh-Green et al., 2003; Vogel, 2016).

4.4. Clumped Isotopes

The bulk Δ_{47} values of the chimneys vary from 0.611 to 0.702‰ which correspond to temperatures of −7 to 20°C (Table S2 in Supporting Information S1, Figures 6a and 6b). Aragonite from these samples have Δ_{47} values that lie within a slightly lower but similar range (0.604–0.690‰; −3 to 22°C). Calcite, on the other hand, has generally lower Δ_{47} than the bulk samples and aragonite (0.471–0.653‰; 7–78°C) (Tables S2 and S3 in Supporting Information S1, Figures 6a and 6b). Samples from Beehive have the lowest and most variable Δ_{47} while the carbonate veins have the highest and least variable Δ_{47} values. In samples where both aragonite and calcite could be measured individually, calcite has consistently lower Δ_{47} than aragonite (Table S3 in Supporting Information S1, Figure 6a).

4.5. Sr Isotopes

Strontium concentrations and $^{87}Sr/^{86}Sr$ ratios of bulk chimney and vein samples are listed in Table S2 of Supporting Information S1 and plotted in Figure 6c together with literature data (Ludwig et al., 2006; Vogel, 2016). $^{87}Sr/^{86}Sr$ isotope ratios ranging between 0.70732 and 0.70900 broadly increase with Sr concentrations (Figure 6c). Not all samples were analyzed for Sr geochemistry; nevertheless, we observe that samples from the interior have among the lowest concentrations and generally have low $^{87}Sr/^{86}Sr$ and Sr concentrations (e.g., Sombrero, eastern wall chimney Table S2 in Supporting Information S1, Figure 6c). The opposite is true for the exterior of the chimneys, which have among the highest $^{87}Sr/^{86}Sr$ and Sr concentrations (e.g., Marker 2, Figure 6c). There is no clear relationship between the Sr geochemistry of chimneys and veins and their location within the LCHF, and samples taken from each of the vent groups have overlapping ranges of $^{87}Sr/^{86}Sr$ and Sr concentrations. One sample taken further away from the site of active venting at Beehive (LC02454b) has a significantly higher $^{87}Sr/^{86}Sr$ and Sr concentration ($^{87}Sr/^{86}Sr = 0.70878$, 3,889 ppm Sr) than the samples collected directly at the vent ($^{87}Sr/^{86}Sr = 0.70732$ to 0.70785, 808–1,246 ppm Sr). Aragonite separates generally have higher $^{87}Sr/^{86}Sr$ ratios (0.70722–0.70899) and Sr concentrations (2131–9,988 ppm Sr) than calcite separates (0.70661–0.70789; 77–1,552 ppm Sr) (Tables S3 and S4 in Supporting Information S1).

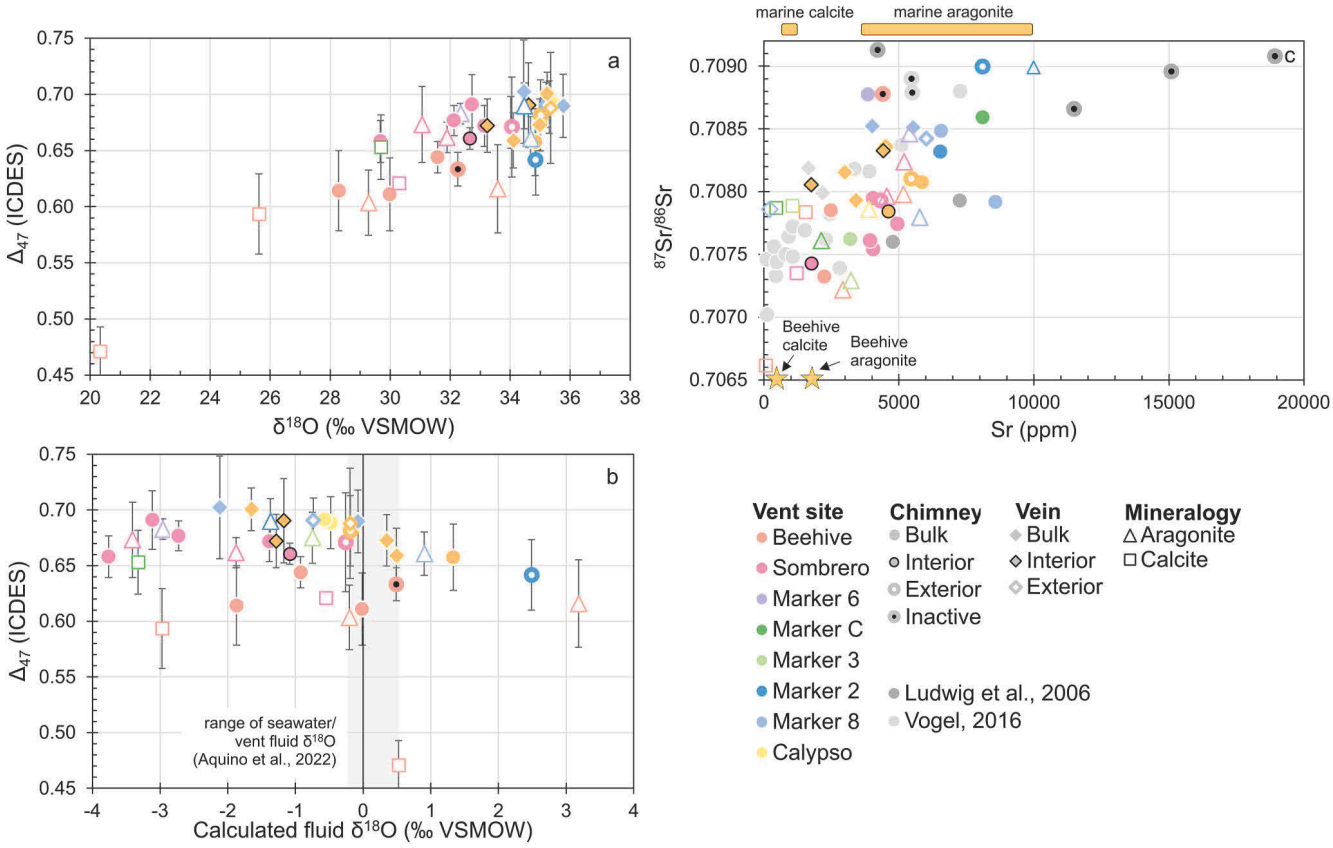

Figure 6. Carbonate clumped isotope compositions and Sr geochemistry of the Lost City chimneys and veins. Δ_{47} values plotted against (a) oxygen isotope compositions and (b) formation fluid oxygen isotope compositions calculated from carbonate clumped isotope compositions. (c) $^{87}Sr/^{86}Sr$ values and Sr concentrations of selected Lost City carbonate samples. Also shown are the range of marine calcite and aragonite from Kinsman (1969). Note: For bulk samples, carbonate Sr contents plotted here are estimated from measured Sr concentrations and the relative abundance of carbonates versus brucite (Table S3 in Supporting Information S1).

5. Discussion

Our results show that the mineralogy and the isotope and element geochemistry of the Lost City hydrothermal chimneys vary spatially within individual chimneys and among different vent sites. In the following section, we first discuss the effect of varying proportions of vent fluid to seawater on the mineralogy of the chimneys and veins. Then, we discuss how rapid and instantaneous precipitation during fluid mixing controls the carbonate carbon, oxygen, and clumped isotope compositions.

5.1. Variable Mixing of Vent Fluid and Seawater

In general, the interior of the chimneys from active vents is brucite(±calcite ± aragonite)-rich, with our scanning electron microscopy data highlighting a spatial association between brucite and calcite (Aquino et al., 2024). The chimney interiors displayed lower $^{87}Sr/^{86}Sr$ values and Sr concentrations than the aragonite-rich exteriors (Figures 3 and 6). This gradient in Sr concentrations and isotopic composition reflects the dominant mineral phases and their affinity to incorporate Sr. The Sr partition coefficient of calcite is lower than that of aragonite (Kinsman, 1969); therefore, the aragonite-dominated chimney exterior is expected to incorporate more Sr (Figure 6c). Moreover, the $^{87}Sr/^{86}Sr$ values of carbonates record the $^{87}Sr/^{86}Sr$ of the fluids from which they precipitate (Coggon & Teagle, 2011). Given that both the endmember hydrothermal fluid ($^{87}Sr/^{86}Sr = 0.70650$, Aquino et al., 2022; Ludwig et al., 2006) and seawater ($^{87}Sr/^{86}Sr = 0.70917$, Palmer & Edmond, 1989) compositions are known, the strontium isotope composition of the carbonates can be used to calculate the mixing proportion of these two fluids during mineral precipitation. Since the temperatures of the vents and seawater are also known, the temperature of the mixed fluid can be estimated (see Section 5.3.1). $^{87}Sr/^{86}Sr$ compositions of bulk chimneys and veins suggest mixing of 13%–69% vent fluid with seawater ($n = 22$). Carbonates from the

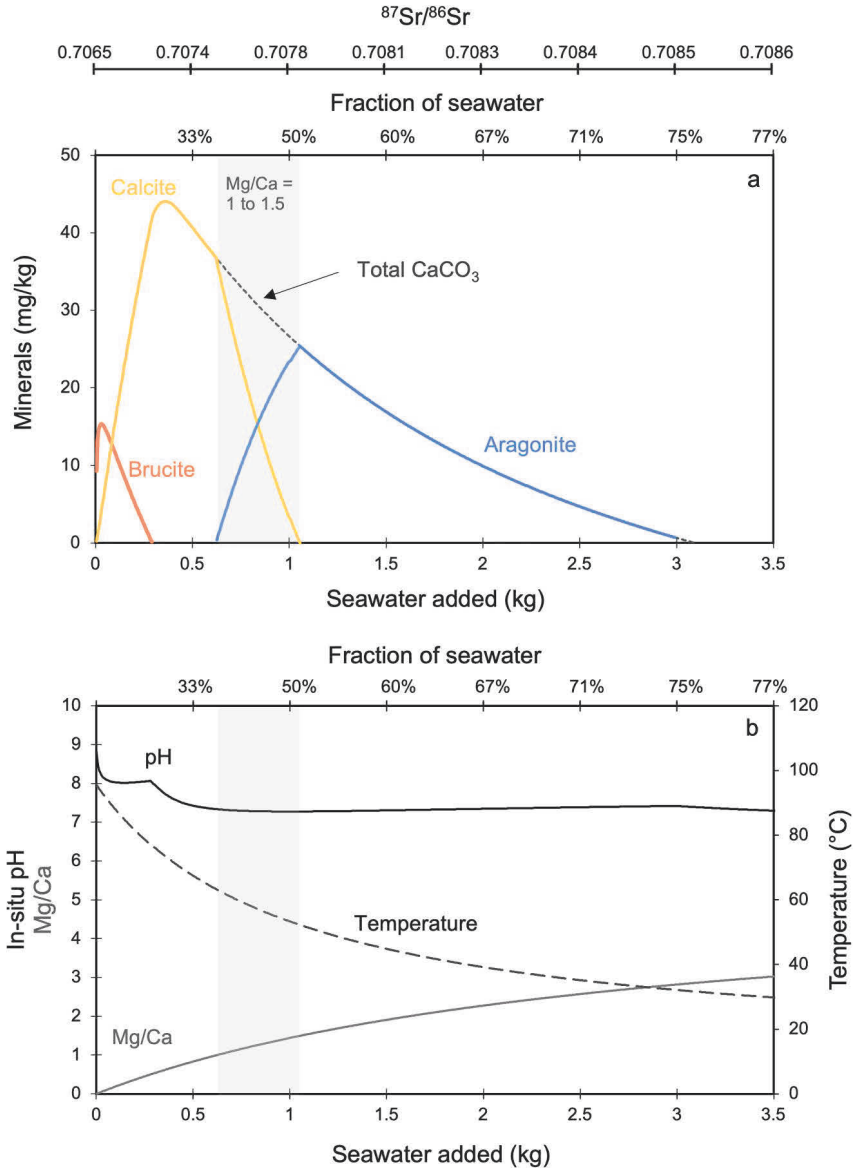

Figure 7. Mixing calculations involving the addition of seawater to 1 kg of Beehive vent fluids. (a) Mixing results in the supersaturation of brucite and calcium carbonate. Brucite solubility is highly sensitive to pH and brucite is saturated only at low seawater fractions <30%. Calcite is stable at lower Mg/Ca ratios whereas aragonite is stable at higher Mg/Ca ratios. (b) Gradients in temperature, pH, and Mg/Ca ratios during mixing. Seawater and Beehive endmember fluid compositons are listed in Table S5 of Supporting Information S1.

chimney interiors generally formed from higher proportions of vent fluid (32%–65% vent fluid; $n = 4$) compared to the exteriors (6%–46% vent fluid; $n = 4$). Calcite is formed from a solution containing 48%–96% vent fluid ($n = 5$) while aragonite is formed with a relatively lower vent fluid contribution (7%–73%; $n = 9$).

To investigate the effect of varying proportions of vent fluid and seawater on chemistry (e.g., Mg/Ca), temperature, pH, and mineral saturation during mixing of seawater and LCHF vent fluids, we calculated a mixing model (Figure 7) using the Geochemist's Workbench® (Bethke et al., 2020). The modeling results show that brucite, aragonite, and/or calcite are supersaturated during the mixing of up to 3 kg of seawater with 1 kg of Beehive vent fluids (up to 75% seawater). Brucite, whose solubility is highly sensitive to pH (Pokrovsky & Schott, 2004), is supersaturated only at <30% seawater where the pH of the solution is predicted to be greater than 8. Note that pH decreases with increasing temperature because of the temperature dependence of the dissociation constant of water (White, 2009). Thus, the actual in situ pH of Beehive vent fluids is lower (8.9) than the pH

measured in the laboratory at 22°C, which is the value commonly reported in the literature (10.8, Table S5 in Supporting Information S1; Aquino et al., 2022; Kelley et al., 2005; Lang et al., 2012). Calcium carbonates, on the other hand, are supersaturated at higher seawater mixing proportions, 0–~50% for calcite, and ~35–~75% seawater for aragonite. This calculation yields comparable results to other studies, which predict the precipitation of brucite at lower seawater fractions and increasing calcium carbonate precipitation with continued seawater admixture (Allen & Seyfried, 2004; Palandri & Reed, 2004).

5.2. Carbonate Mineralogy

The mixing calculation (Figure 7) is consistent with the observation that brucite is generally more abundant in the interior of the structures, while calcium carbonate (Figure 3) is dominant in the exterior. Our petrographic observations suggest that calcite is an early precipitate. In the companion paper (Aquino et al., 2024), we provide mineralogical and textural evidence that the interior of at least some of the chimneys contains significant calcite, whereas their exterior is dominated by aragonite, where a higher proportion of seawater is dominant. Calcite is in most cases intimately associated with brucite and occurs as euhedral, well-formed crystals (Aquino et al., 2024). These mineralogical observations are in agreement with the Sr isotope composition of calcite, which is generally lower (and closer to vent fluid compositions) than those of aragonite (Tables S3 and S4 in Supporting Information S1).

Temperature and fluid Mg/Ca are the main controls on the calcium carbonate polymorph that precipitates from seawater (Berner, 1975; Davis et al., 2000; Morse et al., 1997, 2007; Sun et al., 2015). At 25°C, calcite precipitates when Mg/Ca is below 1.4 ± 0.1 (Morse et al., 1997), while concurrent precipitation of aragonite and calcite is possible at Mg/Ca of around 2 (Sun et al., 2015). This threshold Mg/Ca value for calcite precipitation decreases to about 1 at temperatures >30°C. Based on these considerations, we estimate that for Beehive, co-precipitation of the two calcium carbonate polymorphs is possible at Mg/Ca ratios between ~1 and 1.5 (Figure 7a). Below this Mg/Ca, at very low vent fluid/seawater ratios, calcite can coexist with brucite (Figure 3). With increasing seawater contribution, the Mg/Ca ratio of the fluid is higher than the threshold for calcite precipitation and aragonite precipitates.

The model results are broadly supported by the lower $^{87}Sr/^{86}Sr$ values of calcite (Figure 6c), which imply that calcite precipitates from solutions with more vent fluid, and higher temperatures (calculated from $\delta^{18}O$ and Δ_{47}) than the solutions leading to aragonite formation (Tables S3 and S4 in Supporting Information S1). Overall, the geochemistry and the petrography of calcite in the interior of the chimneys (Aquino et al., 2024) are consistent with calcite being the first carbonate mineral to precipitate in the actively venting structures. The occurrence of primary calcite is not uncommon in hydrothermal chimneys and veins. For example, the interior of active hydrothermal chimneys from the Shinkai Seep Field in the southern Mariana forearc have also been reported to contain more calcite than aragonite (Okumura et al., 2016), and brucite-calcite hydrothermal veins were inferred to form in a fluid-mixing zone at a Lost City-type hydrothermal system at the Iberian Margin (Klein et al., 2015). Furthermore, chimneys from the Old City hydrothermal field (Southwest Indian Ridge), like those from the LCHF, are composed of variable mixtures of brucite, calcite, and aragonite including a sample from an active structure comprising brucite and calcite (Lecoeuvre et al., 2020).

Calcite is also abundant in chimneys from the eastern wall and in veins (Figure 3). Veins have calcite contents of up to 39%, while samples from Calypso and other small chimneys in the eastern wall contain up to 24% and 58% calcite, respectively (Table S2 in Supporting Information S1). We suggest that the relatively low vent temperatures (~30°C for Calypso, 11°C for the vein on the carbonate cap) may explain the abundance of calcite. Mixing small amounts of cold seawater with these relatively low temperature vent fluids will bring the fluid temperatures to <30°C at which the minimum Mg/Ca ratio for aragonite precipitation is higher (Morse et al., 1997).

In addition to the effects of the variation in the mixing proportions of seawater and hydrothermal fluid, carbonate mineralogy and Sr geochemistry in the hydrothermal chimneys are affected by the aging of the structures. Observations from both active and inactive chimneys indicate that aragonite in young, active chimneys is converted to calcite by reaction with seawater over time (Aquino et al., 2024; Ludwig et al., 2006). Ludwig et al. (2006) and Vogel (2016) have shown that active chimneys have generally lower $^{87}Sr/^{86}Sr$ and Sr concentrations (average 6,328 ppm) than inactive structures where Sr concentrations increase (average 9,015 ppm) and $^{87}Sr/^{86}Sr$ ratios approach those of seawater.

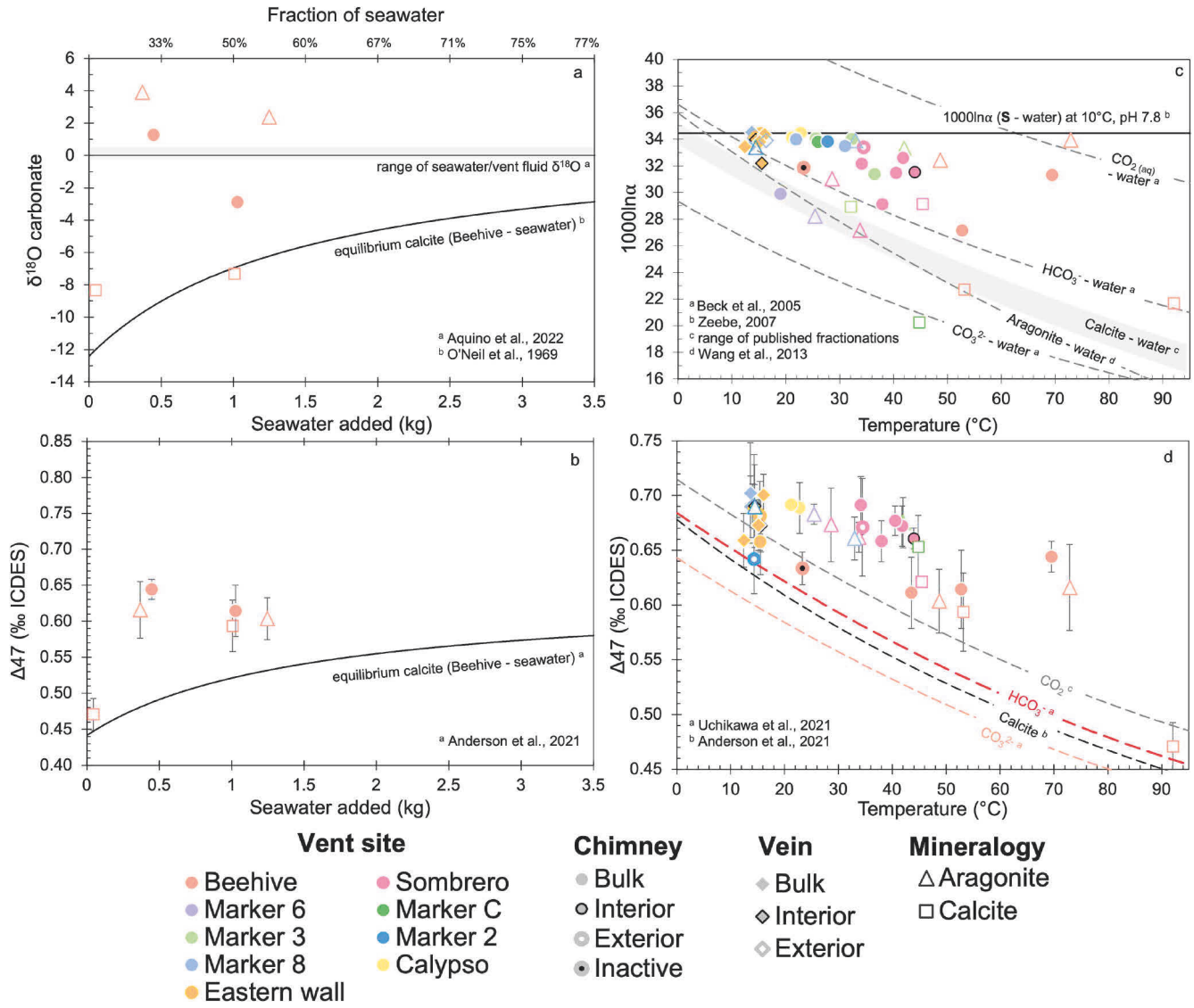

Figure 8. Effect of seawater mixing and temperature on the equilibrium oxygen isotope and clumped isotope compositions. Expected (a) $\delta^{18}O$ and (b) Δ_{47} values of carbonate produced by mixing seawater and Beehive vent fluids assuming equilibrium conditions. Also shown are $\delta^{18}O$ and Δ_{47} values of aragonite, calcite, and bulk samples from Beehive plotted against the fraction of seawater estimated from $^{87}Sr/^{86}Sr$ in the carbonates. Note that for both $\delta^{18}O$ and Δ_{47}, samples from Beehive do not appear to have precipitated in equilibrium. (c) Oxygen isotope fractionation ($1000ln\alpha$) between carbonate and water (vent fluid-seawater solution) of the Lost City carbonate samples plotted against estimated temperature during carbonate precipitation (T_{est}). Also shown are equilibrium fractionation lines between calcite and various dissolved inorganic carbon (DIC) species and water. **S** refers to the overall oxygen isotope fractionation between the sum of the DIC species and water at the pH and temperature of the background seawater at Lost City. (d) Carbonate clumped isotope composition of the Lost City samples plotted against estimated temperatures (T_{est}). Also shown are Δ_{47} values at equilibrium. Temperature is estimated from $^{87}Sr/^{86}Sr$ derived vent fluid fractions and measured vent temperatures (T_{est}, see Section 5.3.1). [c]Upper and lower limits for the calcite-water fractionation are from Coplen (2007) and O'Neil et al. (1969), respectively.

5.3. Multiple Controls on $\delta^{13}C$, $\delta^{18}O$, and Δ_{47} Values

Dissolved inorganic carbon (DIC) in the carbonate system exists in three main forms: $CO_{2(aq)}$ (aqueous carbon dioxide), HCO_3^- (bicarbonate), and CO_3^{2-} (carbonate ion), with the relative proportion of these species changing with pH (Zeebe & Wolf-Gladrow, 2001). The oxygen isotope fractionation between each species and water is different for each DIC species and is dependent on temperature (Figure 8c) (Beck et al., 2005). Therefore, the overall oxygen isotope fractionation between the sum of the DIC species (denoted as **S**, Figure 8c) and water is a function of both pH and temperature (Zeebe, 2007). At Lost City, carbonates are formed during mixing of seawater and vent fluids with different endmember pH, temperature, and chemistry (Kelley et al., 2005; Lang et al., 2012; Ludwig et al., 2006; Proskurowski et al., 2006). Therefore, multiple factors, including variable

mixing proportions of vent fluid and seawater, and the initial pH, temperature, and stable isotope compositions of the vent fluid are expected to affect the compositions of the carbonates.

5.3.1. Estimation of the Temperature of the Mixed Fluid

The carbonates show a large range in $\delta^{18}O$ and Δ_{47} values (Figures 5 and 6). Precipitation temperatures calculated from clumped and oxygen isotope analysis range from −7–78°C to −1–76°C, respectively (Tables S2 and S3 in Supporting Information S1). These calculated temperatures are below the measured vent fluid temperatures (Table S1 in Supporting Information S1), which is expected as the carbonates precipitate from a mixture of vent fluid and seawater (Ludwig et al., 2006; see Section 5.1). However, a significant number of samples yield precipitation temperatures below that of ambient seawater (~10°C; Aquino et al., 2022; Ludwig et al., 2006) and even below zero, indicating precipitation under disequilibrium conditions. We can estimate the temperature of the mixed fluid that produced each carbonate (T_{est}) by combining the $^{87}Sr/^{86}Sr$- derived seawater and vent-fluid fractions (see Section 5.1) with the measured exit temperatures of the vent fluids and the temperature of ambient seawater (Figure 6c, Table S1 in Supporting Information S1). For veins and chimneys where venting was not observed, we used a venting temperature of 22°C, measured in an eastern wall vein northeast of Marker 7 (Aquino et al., 2022). Using this approach, we calculated the expected $\delta^{18}O$ and Δ_{47} of a carbonate that precipitated in equilibrium with this mixed fluid (black line in Figures 8a and 8b for Beehive). Beehive carbonates have $\delta^{18}O$ and Δ_{47} values that are much higher than expected at equilibrium (Figures 8a and 8b). Calcite, however, appears to precipitate closer to equilibrium than aragonite and the bulk sample.

The oxygen isotope fractionation between the carbonates and water ($1000\ln\alpha_{(CaCO3\text{-}H2O)}$; calculated from the $\delta^{18}O$ of the vent fluids and background seawater, Aquino et al., 2022) and Δ_{47} values versus T_{est} for the samples with $^{87}Sr/^{86}Sr$ data are shown in Figures 8c and 8d. Also shown are the equilibrium oxygen isotope fractionation curves between water (i.e., mixture between seawater and vent fluids) and the different DIC species, the sum of all species (S), calcite, and aragonite. Most samples have oxygen and clumped isotope compositions far from the expected equilibrium values of calcite at their estimated formation temperature (Figures 8c and 8d). For $1000\ln\alpha_{(CaCO3\text{-}H2O)}$, most of the data fall between the equilibrium HCO_3^- and CO_3^{2-} compositions at 10°C, the temperature of background seawater at Lost City. Exceptions to this are several calcite samples from Beehive and Marker C, which show lower values. A similar observation is made for Δ_{47}, but for fewer samples.

5.3.2. Disequilibrium Precipitation

Calcium carbonate minerals often precipitate under non-equilibrium conditions in laboratory and most natural settings and thus display $\delta^{18}O$ values that deviate from equilibrium (Daëron et al., 2019; Tripati et al., 2015; Watkins et al., 2013). Disequilibrium, kinetic isotope effects are due to crystal growth reactions as well as the slow isotope exchange between DIC species and water relative to mineral precipitation (Daëron et al., 2019; Watkins et al., 2013; Zeebe et al., 1999). Carbonate minerals at Lost City precipitate very rapidly, whereas isotope equilibrium between DIC and H_2O may take hours to several days to be achieved, especially at higher pH (Dietzel et al., 2009; Watkins et al., 2013; Zeebe & Wolf-Gladrow, 2001; Zeebe et al., 1999).

Oxygen atoms that are incorporated into the carbonate minerals at Lost City are sourced from seawater DIC and/or vent fluid-derived $OH^-_{(aq)}$:

$$\underset{\text{seawater}}{CO_2} + \underset{\text{vent fluid}}{OH^-} \leftrightarrows HCO_3^-, \tag{5}$$

$$\underset{\text{seawater}}{HCO_3^-} + \underset{\text{vent fluid}}{OH^-} \leftrightarrows CO_3^{2-} + H_2O, \tag{6}$$

$$Ca^{2+} + CO_3^{2-} \rightarrow CaCO_3. \tag{7}$$

As described above, the carbonates record oxygen and clumped isotope compositions that are mostly higher than the equilibrium values for calcite (Figures 8c and 8d). Kinetic isotope effects during CO_2 hydroxylation (Equation 5) reported in terrestrial hyperalkaline systems (including natural springs and laboratory experiments) where atmospheric CO_2 is the principal source of carbon produce strong depletions in ^{18}O and ^{13}C (Clark

et al., 1992; Schwarzenbach, Lang, et al., 2013), which is the opposite of what we observe at Lost City. In contrast to terrestrial hyperalkaline springs, seawater DIC which is mostly in the form of HCO_3^- is the principal source of carbon at Lost City.

Quantitative precipitation of seawater DIC at 10°C and pH = 7.8 produced a carbonate with a $1000\ln\alpha_{(CaCO3\text{-}H2O)}$ value of 34.5 (Figure 8c). A number of samples, especially from relatively low temperature vents (e.g., eastern wall, Calypso, Marker 8), seem to record the $\delta^{18}O$ of DIC of background seawater with little variability in $1{,}000\ln\alpha_{(CaCO3\text{-}H2O)}$ across many vents (Figure 8c). The addition of warm (~20–96°C) Ca-OH vent fluids to isotopically equilibrated seawater at 10°C will increase the temperature and pH of the solution and will promote the forward reaction in Equation 6 forming CO_3^{2-} that can be rapidly incorporated into a growing crystal prior to isotope equilibration at the new fluid temperature. Our data show, especially for the samples from the lower temperature vents, that seawater DIC behaves as a generally closed system, and that there is no or very limited reaction between DIC and H_2O or OH^- preceeding carbonate precipitation. In addition, since Ca concentrations (10–40 mmol/kg) are significantly higher than DIC contents (0–2 mmol/kg), quantitative precipitation of the DIC may occur. Thus, the carbonates may directly record the $\delta^{18}O$ and Δ_{47} composition of the starting seawater DIC.

The samples from the relatively higher temperature vents (e.g., Beehive, Sombrero), on the other hand, display lower values which can be explained by a combination of multiple processes (Figure 8c). Carbonates forming at relatively higher temperatures generally also form at relatively higher pH (Figure 7b). At higher pH, the oxygen isotope fractionation between DIC and water decreases (Zeebe, 2007) and the equilibration time for oxygen isotopes in DIC increases (Figure S3 in Supporting Information S1; Watkins et al., 2013; Zeebe, 1999). However, the time required for oxygen isotope equilibration also decreases with increasing temperature (Watkins et al., 2013). At 96°C and pH = 8.9 (e.g., Beehive vent fluid), the oxygen isotope equilibration time is relatively short and may take about 17 s (Figure S3 in Supporting Information S1). We suggest that the carbonates from higher temperature and higher pH vents have formed at conditions closer to equilibrium, which explains the overall lower $\delta^{18}O$ compositions, especially for calcite formed from vent fluid-rich fluids. In contrast, carbonates formed at lower temperatures, either because they are from lower temperature vents or they formed from extensive mixing with seawater, need more time to achieve equilibrium (Figure S3 in Supporting Information S1).

In contrast to oxygen isotopes, carbon isotopes achieve equilibrium at time scales on the order of less than 30 s (Zeebe & Wolf-Gladrow, 2001). Serpentinite-hosted systems such as the Lost City are characterized by fluids that are DIC-poor because of the precipitation of carbonate minerals along the flow paths at depth due to the increased pH and/or reduction to hydrocarbons (Cipolli et al., 2004; Delacour et al., 2008; Kelley et al., 2005; Monnin et al., 2014; Proskurowski et al., 2008; Ternieten et al., 2021a, 2021b). Thus, upon mixing with seawater, C is dominantly sourced from seawater DIC. As a result, carbonates collected from actively venting structures at Lost City predominantly record $\delta^{13}C$ within the range of marine carbonates (−2‰ to +2‰; Wefer & Berger, 1991); (Table S2 in Supporting Information S1; Figure 5). However, $\delta^{13}C$ values as low as −7‰ and as high as +13‰ have been previously reported from samples collected near the eastern wall (e.g., active chimney from Wall Marker H; vein near Marker 7; Früh-Green et al., 2003; Kelley et al., 2005; Vogel, 2016). We did not observe such low $\delta^{13}C$ values, instead our samples from the eastern wall generally record the highest $\delta^{13}C$ and $\delta^{18}O$ values. Low $\delta^{13}C$ values observed in some carbonate samples have been explained by methane oxidation and/or incorporation of mantle-derived carbon (Früh-Green et al., 2003; Vogel, 2016).

An interesting aspect of the data is the strong correlation between $\delta^{18}O$ and Δ_{47} values ($R^2 = 0.75$), which indicates a similar control on these isotope systems. As discussed above, most of the samples record the oxygen and carbon isotope composition of seawater DIC. In contrast, most of the samples have Δ_{47} values that are higher than seawater bicarbonate Δ_{47}, dominating the clumped isotope signal. We do not have an explanation for these elevated Δ_{47}. A significantly lower background seawater temperature than what has been measured for more than a decade at Lost City (~10°C, Aquino et al., 2022; Lang et al., 2012; Ludwig et al., 2006), is unlikely. It is worth noting that the Δ_{47} of the individual DIC species, especially HCO_3^-, are not very well constrained. In particular, experimentally derived Δ_{47} values for HCO_3^- determined by Tripati et al. (2015) are 0.03‰ higher than values predicted from theory in the same study. Other factors may also affect the temperature dependence of the equilibrium Δ_{47} values of the DIC species. For example, the presence of cations may slightly increase equilibrium clumped isotope compositions (Hill et al., 2020). Uchikawa et al. (2021) also noted a discrepancy in Δ_{47} values of up to 0.106 and 0.081‰ for HCO_3^- and CO_3^{2-}, respectively, between values derived from ab initio calculations

by Hill et al. (2020) which consider the presence of Na^+ in the solution and experimental results of Tripati et al. (2015). Overall, despite uncertainties in the clumped isotope composition of DIC, our data indicate that a large number of our samples record a similar Δ_{47} composition which may imply a common DIC source pool for most samples, just like for $\delta^{18}O$ and $\delta^{13}C$.

5.3.3. Other Effects

There is no significant difference in $\delta^{13}C$ between aragonite and calcite, although calcite tends to be slightly depleted in ^{13}C relative to aragonite (Tables S3 and S4 in Supporting Information S1; Figure 5b). This can be attributed to the lower isotopic fractionation between calcite and DIC compared to aragonite (Lécuyer et al., 2012; Romanek et al., 1992). Similarly, calcite records lower $\delta^{18}O$ and Δ_{47} values than aragonite (Tables S3, S4, Figures S2a, S2b, and S2e in Supporting Information S1), reflecting higher temperatures of precipitation. Calcite and aragonite crystals taken from the same sample show very heterogeneous isotopic compositions. Individual calcite crystals from Beehive have $\delta^{18}O$ ranging from −12.0 to −3.1‰ and $\delta^{13}C$ between −1.1 and 2.0‰ (Figure S2a in Supporting Information S1). In general, there is a positive correlation between $\delta^{18}O$ and $\delta^{13}C$, especially in calcite (Figures S2a, S2b, S2d, and S2e in Supporting Information S1). We attribute this correlation to local Rayleigh fractionation during progressive carbonate precipitation. Carbonates generally have a lower $\delta^{18}O$ and $\delta^{13}C$ than the DIC from which they precipitate, resulting in a slight enrichment in the isotopic composition of the remaining DIC. Carbonate crystals that subsequently precipitate from this residual mixed fluid are then slightly enriched in $\delta^{18}O$ and $\delta^{13}C$ relative to the earlier-formed carbonate. However, we observed a significantly larger variation in $\delta^{18}O$ relative to $\delta^{13}C$ (~9 vs. ~1‰) in calcite. Vent fluids from Beehive have a pH of 10.7 at 25°C, which is equivalent to about 0.45 mmol/kg of OH^-. We estimate that mixing with less than 20% of seawater is enough to consume the vent fluid-derived OH^- and can locally decrease the pH. The oxygen isotope fractionation between seawater and DIC increases with decreasing pH (Tripati et al., 2015; Zeebe, 2007). Overall, Rayleigh fractionation combined with a local decrease in pH during progressive carbonate precipitation may explain the trend observed in the composition of the mineral separates collected from the same sample.

5.4. Relationship Between Mineralogy and Geochemistry of the Lost City Chimneys

Here, we link our geochemical results with previous mineralogical and textural investigations of the Lost City chimneys (Aquino et al., 2024; Ludwig et al., 2006). The chimneys and veins are characterized by channel wall flow structures which serve as paleofluid flow paths. These mineral channel walls have been shown to be initially composed of brucite in young and active chimneys (Figure 9a; Aquino et al., 2024; Ludwig et al., 2006). Brucite is stable at relatively higher pH (Pokrovsky & Schott, 2004) and precipitates only from solutions dominated by vent fluids predominantly in the interior of the chimneys (Figures 3 and 7). With continued addition of seawater, carbonates may precipitate on the pre-existing brucite layer. Calcite will form at lower Mg/Ca ratios, that is, from high proportions of vent fluid, in the interior of chimney structures and/or channel walls (Figures 7 and 9). The coprecipitation of brucite and calcite from vent fluid-rich solutions is consistent with the observed association of these minerals at multiple vent locations (Aquino et al., 2024). Aragonite, in contrast, precipitates from solutions with higher Mg/Ca ratios and nucleates more commonly toward the exterior of brucite mineral channel walls from a seawater-dominated fluid (Figure 9a). Our interpretation that primary calcite and aragonite precipitate from distinct solutions is supported by the textural investigation of a fresh spire from the active venting site Calypso. In this sample, both aragonite and calcite were observed to be present, but they precipitated on opposite sides of the brucite channel walls (Figure 9a). Mineral separates were unavailable for this sample because of the small size of the crystals (<50 μm). Nevertheless, calcite in most samples has overall lower $^{87}Sr/^{86}Sr$, $\delta^{18}O$, and Δ_{47} values, indicating formation from generally more undiluted hydrothermal fluid at higher temperatures compared to coexisting aragonite (Figures 5b and 6). Overall, these suggest that the channel walls separate the chimney structure into distinct domains which may allow solutions of different compositions to flow and distinct carbonate minerals to precipitate.

Aquino et al. (2024) also reported brucite minerals that nucleated upon earlier-formed aragonite or calcite crystals. As brucite is supersaturated only at vent-fluid rich solutions, this brucite may form from a new influx of vent fluid (Figure 9b), showing a dynamic fluid circulation through the chimneys. The mineral channel walls thicken as mineral precipitation continues with the mineral assemblage being controlled by the changing composition of the fluid (Figure 9c). Overtime, as hydrothermal activity wanes, brucite and calcite are no longer

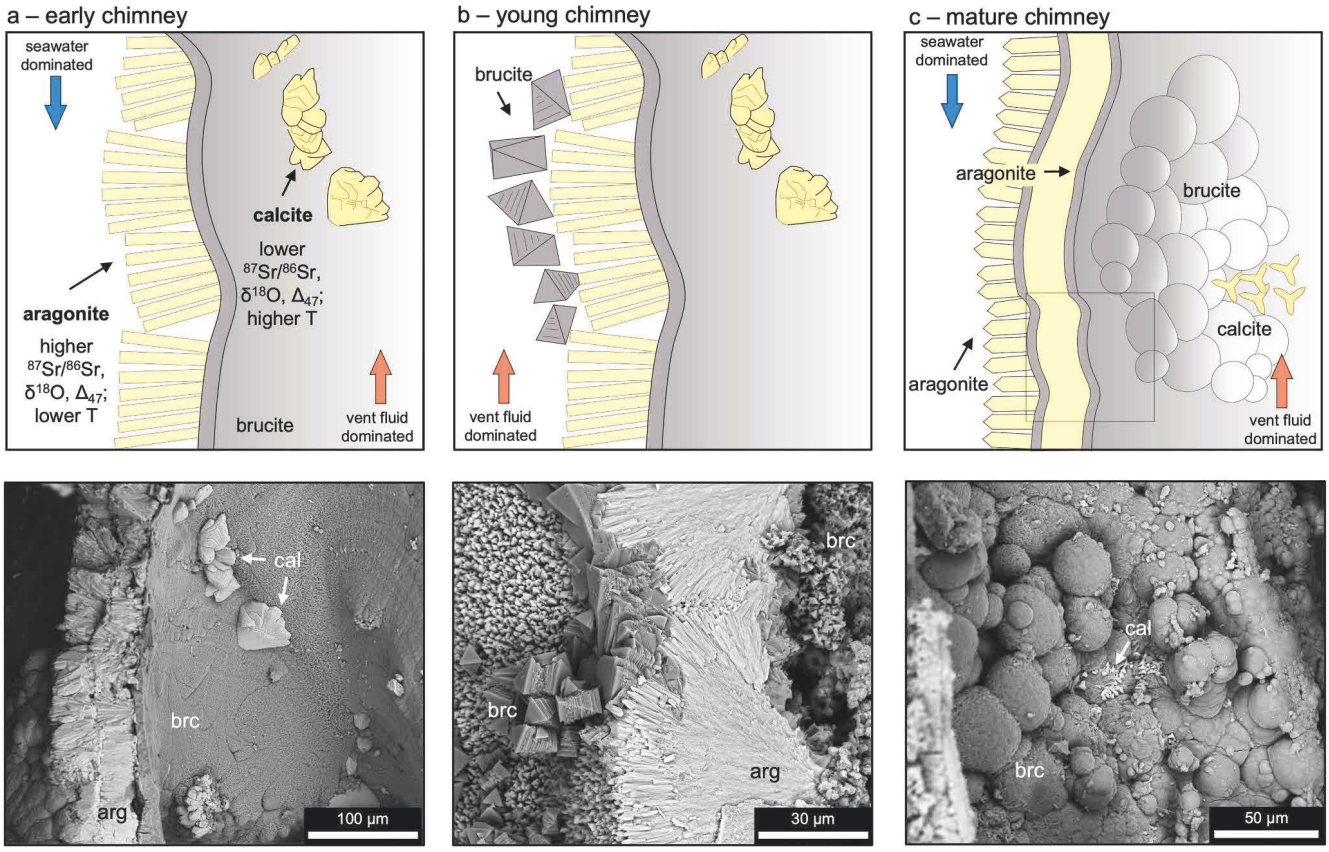

Figure 9. A conceptual model of mineral precipitation in young, active chimneys modified from Aquino et al. (2024). (a) Chimneys initially form brucite mineral membranes that bound fluid flow paths. Carbonate minerals precipitate on these channel walls. In vent fluid-dominated zones, calcite is the carbonate mineral that forms, while aragonite precipitates in seawater-dominated zones. (b and c) Multiple venting events and mixing with seawater lead to the thickening of the channel wall by the precipitation of brucite on earlier formed aragonite or continued aragonite precipitation, depending on the vent fluid-seawater mixing proportions. Box shows the approximate area drawn in (a) and (b). Lower row shows corresponding scanning electron images from Aquino et al. (2024).

thermodynamically stable and only aragonite precipitates. After hydrothermal fluid circulation ceases, the previously formed aragonite is converted to secondary calcite (Ludwig et al., 2006).

6. Conclusions

Hydrothermal chimneys collected from actively venting structures at the LCHF are composed of variable mixtures of brucite, calcite, and aragonite. Brucite is the first mineral to form upon mixing of the hydrothermal fluid with seawater forming an intricate channel system bounded by mineral membrane walls. During continued formation of the chimney, carbonate minerals precipitate on the preexisting channel walls from fluids of varying composition that impart a strong inhomogeneity to the mineralogy and isotope geochemistry of the towers. The mineralogy of the precipitating carbonate depends on the Mg/Ca ratio of the mixed fluid which is controlled by variation in the amount of vent fluid and seawater in the mixed fluid, which can be estimated using $^{87}Sr/^{86}Sr$. Vent fluid-dominated solutions have low Mg/Ca ratios and primarily precipitate brucite and calcite. In contrast, in seawater-dominated environments, chimney structures are often dominated by aragonite. Most carbonates, especially those from relatively lower temperature vents, record the $\delta^{18}O$ of seawater bicarbonate at background seawater temperature (~10°C) and have $\delta^{13}C$ compositions within the range of marine carbonates. The clumped isotope compositions, on the other hand, are within a narrow range above the composition of seawater bicarbonate. Overall, our stable isotope data suggest that at Lost City, DIC is often quantitatively precipitated during fluid mixing, and oxygen isotope equilibration between DIC and H_2O or OH^- does not occur. As a result, the carbonates record oxygen and clumped isotope compositions that do not reflect the temperature of the formation.

Data Availability Statement

Individual analyses of samples are available at the ETH Zurich Research Collection (Aquino, 2022). This study used the Geochemist's Workbench 2020 Standard version (Bethke et al., 2020) (https://www.gwb.com/standard.php).

Acknowledgments
We thank the captain and crew of the R/V Atlantis, ROV Jason, and the scientific party of the 2018 expedition AT42-01. Funding was provided by NSF awards OCE-1536702/1536405/1535962, the Swiss National Science Foundation project No. 200021_163187, the Joint Institute for the Study of the Atmosphere and Ocean (JISAO) under NOAA Cooperative Agreement NA15OAR4320063—Contribution No. 2021-1132, the Deep Carbon Observatory, and the Philippine Department of Science and Technology–Science Education Institute (DOST-SEI). We thank Madalina Jaggi and Stewart Bishop for their assistance during the stable isotope analyses. We also thank James Watkins for providing the curves in Figure S3 of Supporting Information S1 and for discussions that helped improve the manuscript. We appreciate the constructive comments and reviews of Benjamin Tutolo and Alexander Diehl that improved the scholarship of our manuscript.

References

Abrajano, T. A., Sturchio, N. C., Bohlke, J. K., Lyon, G. L., Poreda, R. J., & Stevens, C. M. (1988). Methane-hydrogen gas seeps, Zambales Ophiolite, Philippines: Deep or shallow origin? *Chemical Geology*, *71*(1–3), 211–222. https://doi.org/10.1016/0009-2541(88)90116-7

Allen, D. E., & Seyfried, W. E. (2004). Serpentinization and heat generation: Constraints from Lost City and Rainbow hydrothermal systems. *Geochimica et Cosmochimica Acta*, *68*(6), 1347–1354. https://doi.org/10.1016/j.gca.2003.09.003

Amend, J. P., McCollom, T. M., Hentscher, M., & Bach, W. (2011). Catabolic and anabolic energy for chemolithoautotrophs in deep-sea hydrothermal systems hosted in different rock types. *Geochimica et Cosmochimica Acta*, *75*(19), 5736–5748. https://doi.org/10.1016/j.gca.2011.07.041

Anderson, N. T., Kelson, J. R., Kele, S., Daëron, M., Bonifacie, M., Horita, J., et al. (2021). A Unified Clumped Isotope Thermometer Calibration (0.5–1,100°C) using carbonate-based standardization. *Geophysical Research Letters*, *48*(7), 1–11. https://doi.org/10.1029/2020GL092069

Aquino, K. A. (2022). Fluid mixing and spatial geochemical variability in the Lost City hydrothermal field chimneys (Research data) [Dataset]. ETHZ Research Collection. https://doi.org/10.3929/ethz-b-000579720

Aquino, K. A., Früh-Green, G. L., Bernasconi, S. M., Bontognali, T., Foubert, A., & Lang, S. Q. (2024). Controls on mineral formation in high pH fluids from the Lost City hydrothermal field. *Geochemistry, Geophysics, Geosystems*, *25*, e2023GC011010. https://doi.org/10.1029/2023GC011010

Aquino, K. A., Früh-Green, G. L., Rickli, J., Bernasconi, S. M., Lang, S. Q., Lilley, M. D., & Butterfield, D. A. (2022). Multi-stage evolution of the Lost City hydrothermal vent fluids. *Geochimica et Cosmochimica Acta*, *332*, 239–262. https://doi.org/10.1016/j.gca.2022.06.027

Beck, W. C., Grossman, E. L., & Morse, J. W. (2005). Experimental studies of oxygen isotope fractionation in the carbonic acid system at 15°, 25°, and 40°C. *Geochimica et Cosmochimica Acta*, *69*(14), 3493–3503. https://doi.org/10.1016/j.gca.2005.02.003

Bernasconi, S. M., Bergmann, K. D., Bonifacie, M., Meckler, A. N., Affek, H. P., Bajnai, D., et al. (2021). InterCarb: A community effort to improve interlaboratory standardization of the carbonate clumped isotope thermometer using carbonate standards. *Geochemistry, Geophysics, Geosystems*, *22*(5), e2020GC009588. https://doi.org/10.1029/2020GC009588

Bernasconi, S. M., Müller, I. A., Bergmann, K. D., Breitenbach, S. F. M., Fernandez, A., Hodell, D. A., et al. (2018). Reducing uncertainties in carbonate clumped isotope analysis through consistent carbonate-based standardization. *Geochemistry, Geophysics, Geosystems*, *19*(9), 2895–2914. https://doi.org/10.1029/2017GC007385

Berndt, M. E., Allen, D. E., & Seyfried, W. E. (1996). Reduction of CO_2 during serpentinization of olivine at 300°C and 500 bar. *Geology*, *24*(4), 351–354. https://doi.org/10.1130/0091-7613(1996)024<0351:ROCDSO>2.3.CO;2

Berner, R. A. (1975). The role of magnesium in the crystal growth of calcite and aragonite from sea water. *Geochimica et Cosmochimica Acta*, *39*(4), 489–504. https://doi.org/10.1016/0016-7037(75)90102-7

Bethke, C. M., Farrel, B., & Sharifi, M. (2020). *GWB Essentials Guide*. Aqueous Solutions, LLC Champaign.

Bischoff, J. L. (1968). Kinetics of calcite nucleation: Magnesium ion inhibition and ionic strength catalysis. *Journal of Geophysical Research*, *73*(10), 3315–3322. https://doi.org/10.1029/jb073i010p03315

Blackmann, D. K., Karson, J. A., Kelley, D. S., Cann, J. R., Früh-Green, G. L., Gee, J. S., et al. (2002). Geology of the Atlantis Massif (Mid-Atlantic Ridge, 30°N): Implications for the evolution of an ultramafic oceanic core complex. *Marine Geophysical Research*, *23*(5–6), 443–469. https://doi.org/10.1023/b:mari.0000018232.14085.75

Brazelton, W. J., Schrenk, M. O., Kelley, D. S., & Baross, J. A. (2006). Methane- and sulfur-metabolizing microbial communities dominate the lost city hydrothermal field ecosystem. *Applied and Environmental Microbiology*, *72*(9), 6257–6270. https://doi.org/10.1128/AEM.00574-06

Breitenbach, S. F. M., & Bernasconi, S. M. (2011). Carbon and oxygen isotope analysis of small carbonate samples (20 to 100 µg) with a GasBench II preparation device. *Rapid Communications in Mass Spectrometry*, *25*(13), 1910–1914. https://doi.org/10.1002/rcm.5052

Charlou, J. L., Donval, J. P., Fouquet, Y., Jean-Baptiste, P., & Holm, N. (2002). Geochemistry of high H_2 and CH_4 vent fluids issuing from ultramafic rocks at the Rainbow hydrothermal field (36°14′N, MAR). *Chemical Geology*, *191*(4), 345–359. https://doi.org/10.1016/S0009-2541(02)00134-1

Cipolli, F., Gambardella, B., Marini, L., Ottonello, G., & Zuccolini, M. V. (2004). Geochemistry of high-pH waters from serpentinites of the Gruppo di Voltri (Genova, Italy) and reaction path modeling of CO_2 sequestration in serpentinite aquifers. *Applied Geochemistry*, *19*(5), 787–802. https://doi.org/10.1016/j.apgeochem.2003.10.007

Clark, I. D., Fontes, J.-C., & Fritz, P. (1992). Stable isotope disequilibria in travertine from high pH waters: Laboratory investigations and field observations from Oman. *Geochimica et Cosmochimica Acta*, *56*(5), 2041–2050. https://doi.org/10.1016/0016-7037(92)90328-G

Coggon, R. M., & Teagle, D. A. H. (2011). Hydrothermal calcium-carbonate veins reveal past ocean chemistry. *TrAC, Trends in Analytical Chemistry*, *30*(8), 1252–1268. https://doi.org/10.1016/j.trac.2011.02.011

Coplen, T. B. (2007). Calibration of the calcite-water oxygen-isotope geothermometer at Devils Hole, Nevada, a natural laboratory. *Geochimica et Cosmochimica Acta*, *71*(16), 3948–3957. https://doi.org/10.1016/j.gca.2007.05.028

Daëron, M., Drysdale, R. N., Peral, M., Huyghe, D., Blamart, D., Coplen, T. B., et al. (2019). Most Earth-surface calcites precipitate out of isotopic equilibrium. *Nature Communications*, *10*(1), 1–7. https://doi.org/10.1038/s41467-019-08336-5

Davis, K. J., Dove, P. M., & De Yoreo, J. J. (2000). The role of Mg^{2+} as an impurity in calcite growth. *Science*, *290*(5494), 1134–1137. https://doi.org/10.1126/science.290.5494.1134

Delacour, A., Früh-Green, G. L., Bernasconi, S. M., Schaeffer, P., & Kelley, D. S. (2008). Carbon geochemistry of serpentinites in the Lost City Hydrothermal System (30°N, MAR). *Geochimica et Cosmochimica Acta*, *72*(15), 3681–3702. https://doi.org/10.1016/j.gca.2008.04.039

Delany, J. M., & Lundeen, S. R. (1990). The LLNL thermochemical database.

Deniel, C., & Pin, C. (2001). Single-stage method for the simultaneous isolation of lead and strontium from silicate samples for isotopic measurements. *Analytica Chimica Acta*, *426*(1), 95–103. https://doi.org/10.1016/S0003-2670(00)01185-5

de Souza, G. F., Reynolds, B. C., Kiczka, M., & Bourdon, B. (2010). Evidence for mass-dependent isotopic fractionation of strontium in a glaciated granitic watershed. *Geochimica et Cosmochimica Acta*, *74*(9), 2596–2614. https://doi.org/10.1016/j.gca.2010.02.012

Dick, J. M., & Shock, E. L. (2021). The release of energy during protein synthesis at ultramafic-hosted submarine hydrothermal ecosystems. *Journal of Geophysical Research: Biogeosciences*, *126*(11), e2021JG006436. https://doi.org/10.1029/2021jg006436

Diehl, A., & Bach, W. (2020). MARHYS (MARine HYdrothermal Solutions) database: A global compilation of marine hydrothermal vent fluid, end member, and seawater compositions. *Geochemistry, Geophysics, Geosystems*, *21*(12), e2020GC009385. https://doi.org/10.1029/2020GC009385

Dietzel, M., Tang, J., Leis, A., & Köhler, S. J. (2009). Oxygen isotopic fractionation during inorganic calcite precipitation—Effects of temperature, precipitation rate and pH. *Chemical Geology*, *268*(1–2), 107–115. https://doi.org/10.1016/j.chemgeo.2009.07.015

Douville, E., Charlou, J. L., Oelkers, E. H., Bienvenu, P., Jove Colon, C. F., Donval, J. P., et al. (2002). The rainbow vent fluids (36°14′N, MAR): The influence of ultramafic rocks and phase separation on trace metal content in Mid-Atlantic Ridge hydrothermal fluids. *Chemical Geology*, *184*(1–2), 37–48. https://doi.org/10.1016/S0009-2541(01)00351-5

Eickenbusch, P., Takai, K., Sissman, O., Suzuki, S., Menzies, C., Sakai, S., et al. (2019). Origin of short-chain organic acids in serpentinite mud volcanoes of the Mariana convergent margin. *Frontiers in Microbiology*, *10*, 1–21. https://doi.org/10.3389/fmicb.2019.01729

Friedman, I., & O'Neil, J. R. (1977). *Data of Geochemistry*, *Chapter KK: Compilation of stable isotope fractionation factors of geochemical interest* (6th ed., p. 117). U.S. Geological Survey Professional Paper 440-KK.

Früh-Green, G. L., Connolly, J. A. D., Plas, A., Kelley, D. S., & Grobéty, B. (2004). Serpentinization of oceanic peridotites: Implications for geochemical cycles and biological activity. *Geophysical Monograph Series*, *144*, 119–136. https://doi.org/10.1029/144GM08

Früh-Green, G. L., Kelley, D. S., Bernasconi, S. M., Karson, J. A., Ludwig, K. A., Butterfield, D. A., et al. (2003). 30,000 years of hydrothermal vent field. *Science*, *301*(5632), 495–498. https://doi.org/10.1126/science.1085582

Früh-Green, G. L., Kelley, D. S., Lilley, M. D., Cannat, M., Chavagnac, V., & Baross, J. A. (2022). Diversity of magmatism, hydrothermal processes and microbial interactions at mid-ocean ridges. *Nature Reviews Earth and Environment*, *3*(12), 852–871. https://doi.org/10.1038/s43017-022-00364-y

German, C. R., & Seyfried, W. E. (2013). *Hydrothermal processes*, *Treatise on Geochemistry* (2nd ed., Vol. 8). Elsevier Ltd. https://doi.org/10.1016/B978-0-08-095975-7.00607-0

Ghosh, P., Adkins, J., Affek, H., Balta, B., Guo, W., Schauble, E. A., et al. (2006). ^{13}C-^{18}O bonds in carbonate minerals: A new kind of paleothermometer. *Geochimica et Cosmochimica Acta*, *70*(6), 1439–1456. https://doi.org/10.1016/j.gca.2005.11.014

Glein, C. R., Baross, J. A., & Waite, J. H. (2015). The pH of Enceladus' ocean. *Geochimica et Cosmochimica Acta*, *162*, 202–219. https://doi.org/10.1016/j.gca.2015.04.017

Grozeva, N. G., Klein, F., Seewald, J. S., & Sylva, S. P. (2020). Chemical and isotopic analyses of hydrocarbon-bearing fluid inclusions in olivine-rich rocks. *Philosophical Transactions. Series A, Mathematical, Physical, and Engineering Sciences*, *378*(2165), 20180431. https://doi.org/10.1098/rsta.2018.0431

Hannington, M. D., De Ronde, C. E. J., & Petersen, S. (2005). Sea-floor tectonics and submarine hydrothermal systems. In *One Hundredth Anniversary Volume* (pp. 111–141). Society of Economic Geologists. https://doi.org/10.5382/AV100.06

Hill, P. S., Schauble, E. A., & Tripati, A. (2020). Theoretical constraints on the effects of added cations on clumped, oxygen, and carbon isotope signatures of dissolved inorganic carbon species and minerals. *Geochimica et Cosmochimica Acta*, *269*, 496–539. https://doi.org/10.1016/j.gca.2019.10.016

Holm, N. G., Oze, C., Mousis, O., Waite, J. H., & Guilbert-Lepoutre, A. (2015). Serpentinization and the formation of H_2 and CH_4 on Celestial Bodies (Planets, Moons, Comets). *Astrobiology*, *15*(7), 587–600. https://doi.org/10.1089/ast.2014.1188

John, C. M., & Bowen, D. (2016). Community software for challenging isotope analysis: First applications of 'Easotope' to clumped isotopes. *Rapid Communications in Mass Spectrometry*, *30*(21), 2285–2300. https://doi.org/10.1002/rcm.7720

Kelley, D. S., & Früh-Green, G. L. (1999). Abiogenic methane in deep-seated mid-ocean ridge environments: Insights from stable isotope analyses. *Journal of Geophysical Research*, *104*(B5), 10439–10460. https://doi.org/10.1029/1999JB900058

Kelley, D. S., & Früh-Green, G. L. (2001). Volatiles in mid-ocean ridge environments. In *Ophiolites and Oceanic Crust, New Insights from Field Studies and the Ocean Drilling Program* (Vol. 349, pp. 237–260). Geological Society of America Special Paper.

Kelley, D. S., Karson, J. A., Blackman, D. K., Früh-Green, G. L., Butterfield, D. A., Lilley, M. D., et al. (2001). An off-axis hydrothermal vent field near the Mid-Atlantic Ridge at 30°N. *Nature*, *412*(6843), 145–149. https://doi.org/10.1038/35084000

Kelley, D. S., Karson, J. A., Früh-Green, G. L., Yoerger, D. R., Shank, T. M., Butterfield, D. A., et al. (2005). A serpentinite-hosted ecosystem: The Lost City hydrothermal field. *Science*, *307*(5714), 1428–1434. https://doi.org/10.1126/science.1102556

Kinsman, D. J. J. (1969). Interpretation of Sr^{2+} concentrations in carbonate minerals and rocks. *SEPM Journal of Sedimentary Research*, *39*(2), 486–508. https://doi.org/10.1306/74D71CB7-2B21-11D7-8648000102C1865D

Klein, F., Grozeva, N. G., & Seewald, J. S. (2019). Abiotic methane synthesis and serpentinization in olivine-hosted fluid inclusions. *Proceedings of the National Academy of Sciences of the United States of America*, *116*(36), 17666–17672. https://doi.org/10.1073/pnas.1907871116

Klein, F., Humphris, S. E., Guo, W., Schubotz, F., Schwarzenbach, E. M., Orsi, W. D., & Karl, D. M. (2015). Fluid mixing and the deep biosphere of a fossil Lost City-type hydrothermal system at the Iberia Margin. *Proceedings of the National Academy of Sciences of the United States of America*, *112*(39), 12036–12041. https://doi.org/10.1073/pnas.1504674112

Labidi, J., Young, E. D. D., Giunta, T., Kohl, I. E. E., Seewald, J., Tang, H., et al. (2020). Methane thermometry in deep-sea hydrothermal systems: Evidence for re-ordering of doubly-substituted isotopologues during fluid cooling. *Geochimica et Cosmochimica Acta*, *288*, 248–261. https://doi.org/10.1016/j.gca.2020.08.013

Lang, S. Q., & Brazelton, W. J. (2020). Habitability of the marine serpentinite subsurface: A case study of the lost city hydrothermal field. *Philosophical Transactions. Series A, Mathematical, Physical, and Engineering Sciences*, *378*(2165), 20180429. https://doi.org/10.1098/rsta.2018.0429

Lang, S. Q., Butterfield, D. A., Schulte, M., Kelley, D. S., & Lilley, M. D. (2010). Elevated concentrations of formate, acetate and dissolved organic carbon found at the Lost City hydrothermal field. *Geochimica et Cosmochimica Acta*, *74*(3), 941–952. https://doi.org/10.1016/j.gca.2009.10.045

Lang, S. Q., Früh-Green, G. L., Bernasconi, S. M., Lilley, M. D., Proskurowski, G., Méhay, S., & Butterfield, D. A. (2012). Microbial utilization of abiogenic carbon and hydrogen in a serpentinite-hosted system. *Geochimica et Cosmochimica Acta*, *92*, 82–99. https://doi.org/10.1016/j.gca.2012.06.006

Lartaud, F., Little, C. T. S., De Rafelis, M., Bayon, G., Dyment, J., Ildefonse, B., et al. (2011). Fossil evidence for serpentinization fluids fueling chemosynthetic assemblages. *Proceedings of the National Academy of Sciences*, *108*(19), 7698–7703. https://doi.org/10.1073/pnas.1009383108

Launay, J., & Fontes, J. C. (1985). Les sources thermales de Prony (Nouvelle-Caledonie) et leurs precipites chimiques. Exemple de formation de brucite primaire. *Geologie de La France*, 83–99.

Lecoeuvre, A., Ménez, B., Cannat, M., Chavagnac, V., & Gérard, E. (2020). Microbial ecology of the newly discovered serpentinite-hosted Old City hydrothermal field (southwest Indian ridge). *ISME Journal*, *15*(3), 818–832. https://doi.org/10.1038/s41396-020-00816-7

Lécuyer, C., Hutzler, A., Amiot, R., Daux, V., Grosheny, D., Otero, O., et al. (2012). Carbon and oxygen isotope fractionations between aragonite and calcite of shells from modern molluscs. *Chemical Geology*, *332–333*, 92–101. https://doi.org/10.1016/j.chemgeo.2012.08.034

Ludwig, K. A., Kelley, D. S., Butterfield, D. A., Nelson, B. K., Früh-Green, G., Fru, G., & Früh-Green, G. (2006). Formation and evolution of carbonate chimneys at the Lost City Hydrothermal Field. *Geochimica et Cosmochimica Acta*, *70*(14), 3625–3645. https://doi.org/10.1016/j.gca.2006.04.016

Ludwig, K. A., Shen, C. C., Kelley, D. S., Cheng, H., & Edwards, R. L. (2011). U-Th systematics and ^{230}Th ages of carbonate chimneys at the Lost City Hydrothermal Field. *Geochimica et Cosmochimica Acta*, *75*(7), 1869–1888. https://doi.org/10.1016/j.gca.2011.01.008

McCollom, T. M. (2007). Geochemical constraints on sources of metabolic energy for chemolithoautotrophy in ultramafic-hosted deep-sea hydrothermal systems. *Astrobiology*, *7*(6), 933–950. https://doi.org/10.1089/ast.2006.0119

McCollom, T. M., & Seewald, J. S. (2007). Abiotic synthesis of organic compounds in deep-sea hydrothermal environments. *Chemical Reviews*, *107*(2), 382–401. https://doi.org/10.1021/cr0503660

McDermott, J. M., Seewald, J. S., German, C. R., & Sylva, S. P. (2015). Pathways for abiotic organic synthesis at submarine hydrothermal fields. *Proceedings of the National Academy of Sciences*, *112*(25), 7668–7672. https://doi.org/10.1073/pnas.1506295112

McKay, C. P., Porco, C. C., Altheide, T., Davis, W. L., & Kral, T. A. (2008). The possible origin and persistence of life on enceladus and detection of biomarkers in the plume. *Astrobiology*, *8*(5), 909–919. https://doi.org/10.1089/ast.2008.0265

Meckler, A. N., Ziegler, M., Millán, M. I., Breitenbach, S. F. M., & Bernasconi, S. M. (2014). Long-term performance of the Kiel carbonate device with a new correction scheme for clumped isotope measurements. *Rapid Communications in Mass Spectrometry*, *28*(15), 1705–1715. https://doi.org/10.1002/rcm.6949

Monnin, C., Chavagnac, V., Boulart, C., Ménez, B., Gérard, M., Gérard, E., et al. (2014). Fluid chemistry of the low temperature hyperalkaline hydrothermal system of Prony bay (New Caledonia). *Biogeosciences*, *11*(20), 5687–5706. https://doi.org/10.5194/bg-11-5687-2014

Moody, J. B. (1976). Serpentinization: A review. *Lithos*, *9*(2), 125–138. https://doi.org/10.1016/0024-4937(76)90030-X

Morse, J. W., Arvidson, R. S., & Lüttge, A. (2007). Calcium carbonate formation and dissolution. *Chemical Reviews*, *107*(2), 342–381. https://doi.org/10.1021/cr050358j

Morse, J. W., Wang, Q., & Tsio, M. Y. (1997). Influences of temperature and Mg: Ca ratio on the mineralogy of $CaCO_3$ precipitated from seawater. *Geology*, *25*(1), 85–87. https://doi.org/10.1130/0091-7613(1997)025<0085:IOTAMC>2.3.CO;2

Müller, I. A., Fernandez, A., Radke, J., van Dijk, J., Bowen, D., Schwieters, J., & Bernasconi, S. M. (2017). Carbonate clumped isotope analyses with the long-integration dual-inlet (LIDI) workflow: Scratching at the lower sample weight boundaries. *Rapid Communications in Mass Spectrometry*, *31*(12), 1057–1066. https://doi.org/10.1002/rcm.7878

Neal, C., & Stanger, G. (1983). Hydrogen generation from mantle source rocks in Oman. *Earth and Planetary Science Letters*, *66*(C), 315–320. https://doi.org/10.1016/0012-821X(83)90144-9

Nier, A. O. (1938). The isotopic constitution of strontium, barium, bismuth, thallium and mercury. *Physical Review*, *54*(4), 275–278. https://doi.org/10.1103/PhysRev.54.275

Ohara, Y., Reagan, M. K., Fujikura, K., Watanabe, H., Michibayashi, K., Ishii, T., et al. (2012). A serpentinite-hosted ecosystem in the Southern Mariana Forearc. *Proceedings of the National Academy of Sciences of the United States of America*, *109*(8), 2831–2835. https://doi.org/10.1073/pnas.1112005109

Okumura, T., Ohara, Y., Stern, R. J., Yamanaka, T., Onishi, Y., Watanabe, H., et al. (2016). Brucite chimney formation and carbonate alteration at the Shinkai Seep Field, a serpentinite-hosted vent system in the southern Mariana forearc. *Geochemistry, Geophysics, Geosystems*, *17*(9), 3775–3796. https://doi.org/10.1002/2016GC006449

O'Neil, J. R., Clayton, R. N., & Mayeda, T. K. (1969). Oxygen isotope fractionation in divalent metal carbonates. *The Journal of Chemical Physics*, *51*(12), 5547–5558. https://doi.org/10.1063/1.1671982

Palandri, J. L., & Reed, M. H. (2004). Geochemical models of metasomatism in ultramafic systems: Serpentinization, rodingitization, and sea floor carbonate chimney precipitation. *Geochimica et Cosmochimica Acta*, *68*(5), 1115–1133. https://doi.org/10.1016/j.gca.2003.08.006

Palmer, M. R., & Edmond, J. M. (1989). The strontium isotope budget of the modern ocean. *Earth and Planetary Science Letters*, *92*(1), 11–26. https://doi.org/10.1016/0012-821X(89)90017-4

Pisapia, C., Gérard, E., Gérard, M., Lecourt, L., Lang, S. Q., Pelletier, B., et al. (2017). Mineralizing filamentous bacteria from the prony bay hydrothermal field give new insights into the functioning of serpentinization-based subseafloor ecosystems. *Frontiers in Microbiology*, *8*, 1–18. https://doi.org/10.3389/fmicb.2017.00057

Pokrovsky, O. S., & Schott, J. (2004). Experimental study of brucite dissolution and precipitation in aqueous solutions: Surface speciation and chemical affinity control. *Geochimica et Cosmochimica Acta*, *68*(1), 31–45. https://doi.org/10.1016/S0016-7037(03)00238-2

Proskurowski, G., Lilley, M. D., Kelley, D. S., & Olson, E. J. (2006). Low temperature volatile production at the Lost City Hydrothermal Field, evidence from a hydrogen stable isotope geothermometer. *Chemical Geology*, *229*(4), 331–343. https://doi.org/10.1016/j.chemgeo.2005.11.005

Proskurowski, G., Lilley, M. D., Seewald, J. S., Früh-Green, G. L., Olson, E. J., Lupton, J. E., et al. (2008). Abiogenic hydrocarbon production at Lost City hydrothermal field. *Science*, *319*(5863), 604–607. https://doi.org/10.1126/science.1151194

Romanek, C. S., Grossman, E. L., & Morse, J. W. (1992). Carbon isotopic fractionation in synthetic aragonite and calcite: Effects of temperature and precipitation rate. *Geochimica et Cosmochimica Acta*, *56*(1), 419–430. https://doi.org/10.1016/0016-7037(92)90142-6

Schauble, E. A., Ghosh, P., & Eiler, J. M. (2006). Preferential formation of ^{13}C-^{18}O bonds in carbonate minerals, estimated using first-principles lattice dynamics. *Geochimica et Cosmochimica Acta*, *70*(10), 2510–2529. https://doi.org/10.1016/j.gca.2006.02.011

Schrenk, M. O., Kelley, D. S., Bolton, S. A., & Baross, J. A. (2004). Low archaeal diversity linked to subseafloor geochemical processes at the Lost City Hydrothermal Field, Mid-Atlantic Ridge. *Environmental Microbiology*, *6*(10), 1086–1095. https://doi.org/10.1111/j.1462-2920.2004.00650.x

Schwarzenbach, E. M., Früh-Green, G. L., Bernasconi, S. M., Alt, J. C., & Plas, A. (2013). Serpentinization and carbon sequestration: A study of two ancient peridotite-hosted hydrothermal systems. *Chemical Geology*, *351*, 115–133. https://doi.org/10.1016/j.chemgeo.2013.05.016

Schwarzenbach, E. M., Lang, S. Q., Früh-Green, G. L., Lilley, M. D., Bernasconi, S. M., & Méhay, S. (2013). Sources and cycling of carbon in continental, serpentinite-hosted alkaline springs in the Voltri Massif, Italy. *Lithos*, *177*, 226–244. https://doi.org/10.1016/j.lithos.2013.07.009

Seyfried, W. E., Pester, N. J., Tutolo, B. M., & Ding, K. (2015). The Lost City hydrothermal system: Constraints imposed by vent fluid chemistry and reaction path models on subseafloor heat and mass transfer processes. *Geochimica et Cosmochimica Acta*, *163*, 59–79. https://doi.org/10.1016/j.gca.2015.04.040

Shock, E. L., & Schulte, M. D. (1998). Organic synthesis during fluid mixing in hydrothermal systems. *Journal of Geophysical Research*, *103*(E12), 28513–28527. https://doi.org/10.1029/98JE02142

Sleep, N. H. (2010). The Hadean-Archaean environment. *Cold Spring Harbor Perspectives in Biology*, *2*(6), 1–14. https://doi.org/10.1101/cshperspect.a002527

Steele, A., Benning, L. G., Wirth, R., Schreiber, A., Araki, T., McCubbin, F. M., et al. (2022). Organic synthesis associated with serpentinization and carbonation on early Mars. *Science*, *375*(6577), 172–177. https://doi.org/10.1126/science.abg7905

Sun, W., Jayaraman, S., Chen, W., Persson, K. A., & Ceder, G. (2015). Nucleation of metastable aragonite $CaCO_3$ in seawater. *Proceedings of the National Academy of Sciences*, *112*(11), 3199–3204. https://doi.org/10.1073/pnas.1423898112

Ternieten, L., Früh-Green, G. L., & Bernasconi, S. M. (2021a). Carbonate mineralogy in mantle peridotites of the Atlantis Massif (IODP Expedition 357). *Journal of Geophysical Research: Solid Earth*, *126*(12), e2021JB021885. https://doi.org/10.1029/2021jb021885

Ternieten, L., Früh-Green, G. L., & Bernasconi, S. M. (2021b). Distribution and sources of carbon in serpentinized mantle peridotites at the Atlantis Massif (IODP Expedition 357). *Journal of Geophysical Research: Solid Earth*, *126*(10), e2021JB021973. https://doi.org/10.1029/2021JB021973

Thirlwall, M. F. (1991). Long-term reproducibility of multicollector Sr and Nd isotope ratio analysis. *Chemical Geology*, *94*(2), 85–104. https://doi.org/10.1016/S0009-2541(10)80021-X

Tripati, A. K., Hill, P. S., Eagle, R. A., Mosenfelder, J. L., Tang, J., Schauble, E. A., et al. (2015). Beyond temperature: Clumped isotope signatures in dissolved inorganic carbon species and the influence of solution chemistry on carbonate mineral composition. *Geochimica et Cosmochimica Acta*, *166*, 344–371. https://doi.org/10.1016/j.gca.2015.06.021

Turekian, K. K., & Wedepohl, K. H. (1961). Distribution of the elements in some major units of the Earth's crust. *GSA Bulletin*, *72*(2), 175–192. https://doi.org/10.1130/0016-7606(1961)72[175:DOTEIS]2.0.CO;2

Uchikawa, J., Chen, S., Eiler, J. M., Adkins, J. F., & Zeebe, R. E. (2021). Trajectory and timescale of oxygen and clumped isotope equilibration in the dissolved carbonate system under normal and enzymatically-catalyzed conditions at 25°C. *Geochimica et Cosmochimica Acta*, *314*, 313–333. https://doi.org/10.1016/j.gca.2021.08.014

Urey, H. C., Lowenstam, H. A., Epstein, S., & McKinney, C. R. (1951). Measurement of paleotemperatures and temperatures and the southeastern United States. *Bulletin of the Geological Society of America*, *62*(4), 399–416. https://doi.org/10.1130/0016-7606(1951)62[399:mopato]2.0.co;2

Vogel, M. (2016). *Peridotite-hosted hydrothermal systems past and present: Serpentinization, metasomatism and carbonate precipitation in modern and jurassic ultramafic seafloor*. ETH Zurich. https://doi.org/10.3929/ethz-a-010679089

Von Damm, K. L. (1990). Seafloor hydrothermal activity: Black smoker chemistry and chimneys. *Annual Review of Earth & Planetary Sciences*, *18*(1), 173–204. https://doi.org/10.1146/annurev.ea.18.050190.001133

Waite, J. H., Glein, C. R., Perryman, R. S., Teolis, B. D., Magee, B. A., Miller, G., et al. (2017). Cassini finds molecular hydrogen in the Enceladus plume: Evidence for hydrothermal processes. *Science*, *356*(6334), 155–159. https://doi.org/10.1126/science.aai8703

Wang, D. T., Reeves, E. P., McDermott, J. M., Seewald, J. S., & Ono, S. (2018). Clumped isotopologue constraints on the origin of methane at seafloor hot springs. *Geochimica et Cosmochimica Acta*, *223*, 141–158. https://doi.org/10.1016/j.gca.2017.11.030

Watkins, J. M., Nielsen, L. C., Ryerson, F. J., & DePaolo, D. J. (2013). The influence of kinetics on the oxygen isotope composition of calcium carbonate. *Earth and Planetary Science Letters*, *375*, 349–360. https://doi.org/10.1016/j.epsl.2013.05.054

Wefer, G., & Berger, W. H. (1991). Isotope paleontology: Growth and composition of extant calcareous species. *Marine Geology*, *100*(1–4), 207–248. https://doi.org/10.1016/0025-3227(91)90234-u

White, W. M. (2009). Chapter 6. Aquatic chemistry, *Geochemistry* (Vol. *210–257*). https://doi.org/10.1109/ISIP.2010.108

Zeebe, R. E. (1999). An explanation of the effect of seawater carbonate concentration on foraminiferal oxygen isotopes. *Geochimica et Cosmochimica Acta*, *63*(13–14), 2001–2007. https://doi.org/10.1016/S0016-7037(99)00091-5

Zeebe, R. E. (2007). An expression for the overall oxygen isotope fractionation between the sum of dissolved inorganic carbon and water. *Geochemistry, Geophysics, Geosystems*, *8*(9), Q09002. https://doi.org/10.1029/2007GC001663

Zeebe, R. E., & Wolf-Gladrow, D. A. (2001). *CO_2 in seawater: Equilibrium, kinetics, isotopes* (Vol. 65). Gulf Professional Publishing.

Zeebe, R. E., Wolf-Gladrow, D. A., & Jansen, H. (1999). On the time required to establish chemical and isotopic equilibrium in the carbon dioxide system in seawater. *Marine Chemistry*, *65*(3–4), 135–153. https://doi.org/10.1016/S0304-4203(98)00092-9